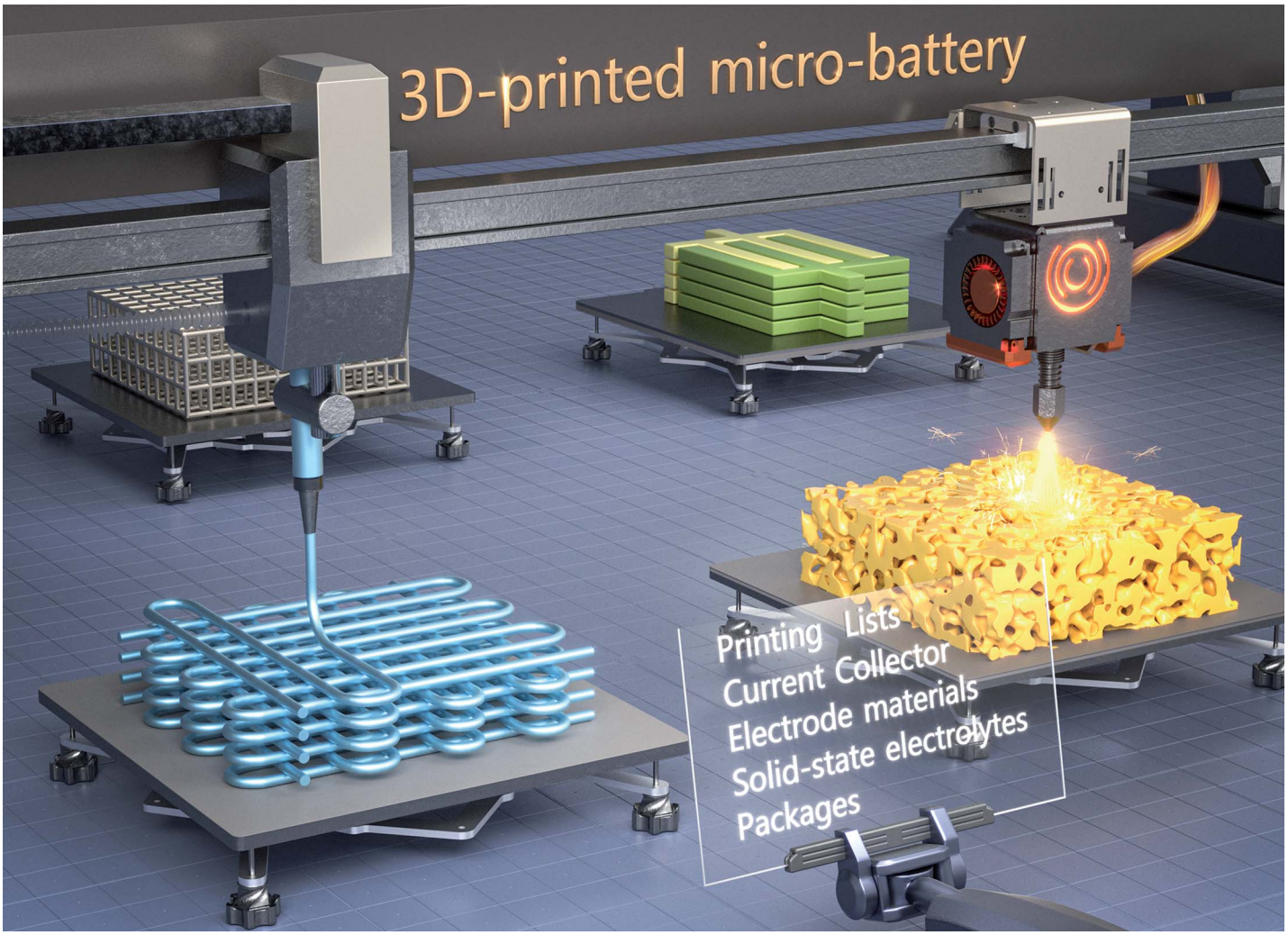

Showcasing research from Professor Zhong-Shuai Wu's laboratory, Dalian Institute of Chemical Physics, Chinese Academy of Sciences, Dalian, China.

The status and challenging perspectives of 3D-printed micro-batteries

In this work, Zhong-Shuai Wu, Shuanghao Zheng and co-workers summarize the latest advances in 3D-printed micro-batteries. They discuss the connection between printable materials and printing techniques, general approaches to make battery modules printable, as well as rational design considerations. Furthermore, upcoming challenges are addressed together with further research directions in terms of novel functional materials, advanced printing technologies, new device designs, reaction mechanisms, and new integrated micro-systems.

As featured in:

See Shuanghao Zheng, Zhong-Shuai Wu *et al.*, *Chem. Sci.*, 2024, **15**, 5451.

ROYAL SOCIETY OF CHEMISTRY

rsc.li/chemical-science

Registered charity number: 207890

Chemical Science

ROYAL SOCIETY OF CHEMISTRY

REVIEW

View Article Online
View Journal | View Issue

Cite this: *Chem. Sci.*, 2024, **15**, 5451

The status and challenging perspectives of 3D-printed micro-batteries

Jiaxin Ma, [ab] Shuanghao Zheng,*[ac] Yinghua Fu,[ad] Xiao Wang,[a] Jieqiong Qin[e] and Zhong-Shuai Wu *[ac]

In the era of the Internet of Things and wearable electronics, 3D-printed micro-batteries with miniaturization, aesthetic diversity and high aspect ratio, have emerged as a recent innovation that solves the problems of limited design diversity, poor flexibility and low mass loading of materials associated with traditional power sources restricted by the slurry-casting method. Thus, a comprehensive understanding of the rational design of 3D-printed materials, inks, methods, configurations and systems is critical to optimize the electrochemical performance of customizable 3D-printed micro-batteries. In this review, we offer a key overview and systematic discussion on 3D-printed micro-batteries, emphasizing the close relationship between printable materials and printing technology, as well as the reasonable design of inks. Initially, we compare the distinct characteristics of various printing technologies, and subsequently emphatically expound the printable components of micro-batteries and general approaches to prepare printable inks. After that, we focus on the outstanding role played by 3D printing design in the device architecture, battery configuration, performance improvement, and system integration. Finally, the future challenges and perspectives concerning high-performance 3D-printed micro-batteries are adequately highlighted and discussed. This comprehensive discussion aims at providing a blueprint for the design and construction of next-generation 3D-printed micro-batteries.

Received 30th December 2023
Accepted 10th March 2024

DOI: 10.1039/d3sc06999k

rsc.li/chemical-science

[a]*State Key Laboratory of Catalysis, Dalian Institute of Chemical Physics, Chinese Academy of Sciences, 457 Zhongshan Road, Dalian 116023, China. E-mail: shuanghao_zheng@dicp.ac.cn; wuzs@dicp.ac.cn*

[b]*School of Materials Science and Engineering, Zhengzhou University, Zhengzhou 450001, China*

[c]*Dalian National Laboratory for Clean Energy, Chinese Academy of Sciences, 457 Zhongshan Road, Dalian 116023, China*

[d]*University of Chinese Academy of Sciences, 19A Yuquan Road, Shijingshan District, Beijing 100049, China*

[e]*College of Science, Henan Agricultural University, No. 63 Agricultural Road, Zhengzhou 450002, China*

Introduction

The impending rise of the Internet of Things (IoT), portable microelectronics, and smart sensors and ever-growing demands for security and sustainability of humanity[1–3] have inspired the pursuit of advanced microscale electrochemical energy storage devices,[4–7] which are envisioned to exhibit high performance and stability, and simultaneously form factor-free, lightweight, customizable, and seamlessly integrated target electronic systems.[8–10] Special emphasis has been given to micro-batteries (MBs) with

Jiaxin Ma

Jiaxin Ma received his PhD from Dalian Institute of Chemical Physics, Chinese Academy of Sciences, under the supervision of Prof. Zhong-Shuai Wu in 2023. Subsequently, he became an Associate Professor at the School of Materials Science and Engineering of Zhengzhou University. His current research is focused on printable micro-scale electrochemical energy storage devices, solid-state batteries and pouch cells.

Shuanghao Zheng

Shuanghao Zheng received his PhD degree from Dalian Institute of Chemical Physics (DICP), Chinese Academy of Sciences, under the supervision of Prof. Xinhe Bao and Prof. Zhong-Shuai Wu. Then, he worked at DICP as an Associate Professor. His research interests focus on MXene, 2D materials, and miniaturized electrochemical energy storage devices.

a higher energy density to ensure prolonged endurance.[11–14] Generally, MBs have a total footprint area in the square millimeter or even square centimeter scale, or electrode thickness limited to 10 μm or sub-cubic-millimeter volumes for 3D configurations. According to the microelectrode geometry, MBs can be categorized as 1D fiber shapes, 2D/3D stacked architectures and 2D/3D planar configurations.[15–17] Different from the conventional batteries with a sandwich-like configuration only allowing ion diffusion along the vertical direction, the unique electrode structure of MBs can shorten the ion transfer pathways, improving the rate capability and power density. Especially, the planar MBs with interdigital microelectrodes exhibit the multi-direction ion diffusion mechanism, greatly facilitating the reaction kinetics.[18,19] Besides, considering the architectural aspect, traditional batteries prepared by the slurry-cast method are difficulty to fit the aesthetic versatility and shape customizability of microelectronics.[20–22] Remarkably, MBs can address the aforementioned problems of shape diversity and tailored structures by virtue of various microfabrication methods, such as photolithography,[23,24] laser scribing,[25–27] electrodeposition,[28,29] screen-printing,[30,31] and 3D printing techniques.[32–34] Photolithography and laser scribing can achieve interdigital patterns on a substrate but suffer from low material utilization.[35,36] Alternatively, screen printing is a fast and convenient fabrication process, but the used inks must be passed through a mask mesh, which makes it difficult to integrate MBs on an irregular substrate such as curved surfaces and spherical structures.[37,38]

Notably, 3D printing, which involves directly manufacturing controllable 3D structures using rationally designed inks, is widely regarded as a promising technique for the fabrication of MBs.[39] This is attributed to its processability, high efficiency, low cost, reproducibility and design diversity.[40–43] 3D printing has been successfully employed to construct MBs,[44,45] possessing the following superiorities: (i) greatly enhancing the design freedom on the microscale and ability to manufacture complex structures, achieving the desired shape;[46,47] (ii) having a higher areal mass loading of materials and larger aspect ratio of electrodes, thereby delivering an increased areal/volumetric energy density;[48,49] (iii) boosting the power density of MBs because of the shorter ion diffusion pathways;[50,51] (iv) greatly improving the material utilization, thus reducing production costs;[52] and (v) direct compatible integration of MBs with microelectronics.[53,54]

Yinghua Fu

Yinghua Fu is a PhD candidate at the Dalian Institute of Chemical Physics, Chinese Academy of Sciences. Her research focuses on 3D printing of micro-electrochemical energy storage devices and the study of energy storage mechanisms.

Jieqiong Qin

Jieqiong Qin received her PhD degree at Dalian Institute of Chemical Physics, Chinese Academy of Sciences from 2016 to 2020, under the supervision of Prof. Zhong-Shuai Wu. Presently, she is a Professor at the College of Science, Henan Agricultural University. Her research focuses on the design and synthesis of 2D mesoporous materials for electrochemical energy storage devices, such as supercapacitors and batteries.

Xiao Wang

Xiao Wang received her PhD degree from Dalian Institute of Chemical Physics (DICP), Chinese Academy of Sciences (CAS), under the supervision of Prof. Zhong-Shuai Wu in 2021 and worked as a Postdoctoral Researcher at DICP, CAS, advised by Prof. Zhong-Shuai Wu. Then, she became an Associate Professor at DICP, CAS. Her research interests focus on graphene and 2D materials, and flexible and planar electrochemical energy storage devices, especially zinc-based batteries.

Zhong-Shuai Wu

Zhong-Shuai Wu received his PhD from the Institute for Metal Research, CAS in 2011, and worked as a Postdoctoral Fellow at the Max Planck Institute for Polymer Research in Mainz, Germany from 2011 to 2015. Subsequently, Dr Wu became a Full Professor at DICP, CAS, and was promoted in 2018 as a DICP Chair Professor. He is a Group Leader of 2D Materials Chemistry & Energy Applications. Currently, Prof. Wu's research interests include graphene and 2D materials, surface electrochemistry and nano-electrochemistry, microscale electrochemical energy storage devices, supercapacitors, batteries, and catalysis. For more information, see ***http://www.zswu.dicp.ac.cn****.*

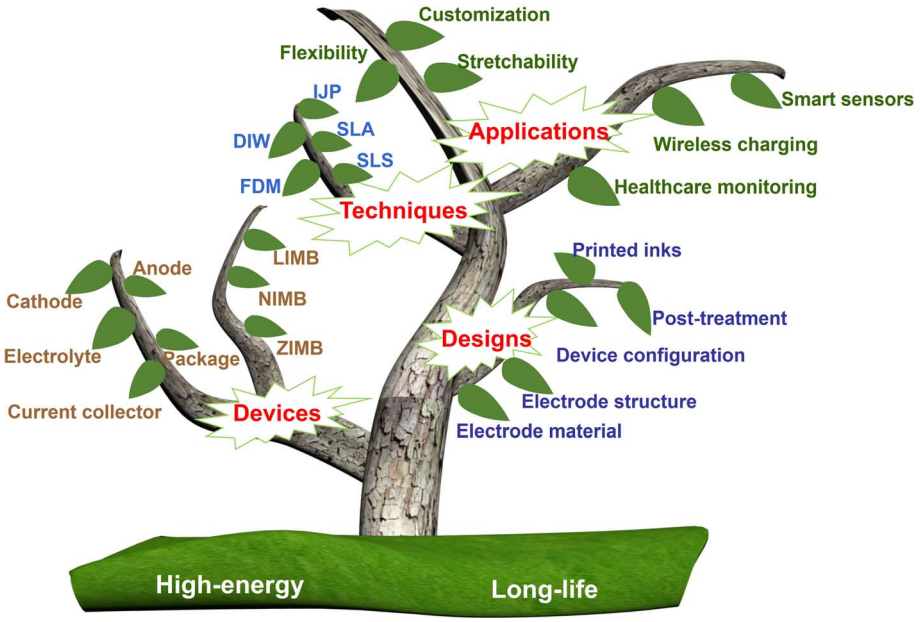

Fig. 1 Overview of 3D-printed MBs including printing techniques, electrode designs, printable devices and their applications.

Current research on 3D-printed MBs mainly focuses on the following aspects: (i) the controllable synthesis of printable inks for the power source components (electrodes, electrolyte, current collector, and separator) with adjustable rheological properties and high electrochemical performances,[55,56] (ii) the construction of high-efficiency ion/electron pathways to overcome the problems of sluggish reaction kinetics and low active material utilization in thick electrodes,[57,58] (iii) the elimination of multiple interfaces in miniaturized devices on the micro-scale,[33,59] (iv) high-precision printing process to achieve a high areal/volumetric capacity/capacitance for the electrode and the establishment of interface compatibility and stability between the electrodes and electrolyte,[60,61] and (v) the high-throughput preparation of printable power sources and high-efficiency/compatibility modular micro-systems.[62,63] The collective achievements in these areas are jointly devoted to constructing fully printed MBs.

Herein, firstly, we present an elaborate introduction of the various 3D printing methods (Fig. 1), including their working principles, advantages, disadvantages, corresponding printing materials and operational processes. Secondly, we summarize the universal printing strategy and printable components of MBs, including cathodes, anodes, electrolytes, current collectors, substrates, separators and packages. Thirdly, the recent advances in 3D-printed MBs are presented, according to the type of charge carriers in the electrolyte, such as lithium-ion MBs (LIMBs), sodium-ion MBs (NIMBs) and zinc-ion MBs (ZIMBs). Finally, we emphasize the key strategies and challenging perspectives of 3D-printed MBs.

3D printing techniques

In the realm of printing processes, 3D printing techniques can be classified into seven types, as follows: (1) material jetting (*e.g.*, inkjet printing (IJP)[64] and aerosol jet printing (AJP)[65]), (2) material extrusion (including direct ink writing (DIW) and fused deposition modeling (FDM)),[66,67] (3) powder bed fusion (*e.g.*, selective laser sintering (SLS)[68] and direct metal laser sintering (DMLS)[69]), (4) vat photopolymerization (*e.g.*, stereolithography (SLA),[70] digital light processing (DLP),[71] and two-photon lithography (TPL)[72]), (5) sheet lamination (*e.g.*, laminated object manufacturing (LOM)),[73] (6) binder jetting,[74] and (7) directed energy deposition (DED).[75] In this review, four representative 3D printing techniques (DIW, FDM, IJP and SLA) specifically applied in the fabrication of MBs are summarized.[76–80] In general, the appropriate printing technology is selected depending on the required materials for the battery module, the characteristics and processability of the final products, and the target architecture and performance goals. Therefore, it is significant to understand the distinctive features of these 3D printing technologies for further material option and technology development. As shown in Fig. 2, the merits and demerits of the four representative printing techniques are compared, including ink requirements, material range, resolution, cost, size, throughput and design versatility. In this section, we carefully analyse four representative 3D printing techniques, *e.g.*, DIW, FDM, IJP and SLA (Table 1).

Direct ink writing

DIW, as an exemplary extrusion-type printing technique, involves the extrusion of viscoelastic inks with the characteristic shear-thinning rheological behavior.[81,82] In the printing process, the prepared inks are transferred to a syringe equipped with a specific needle. Due to the shear-thinning feature, the inks can be extruded into continuous filaments through a nozzle under controlled pressure generated by compressed air, enabling the realization of 3D patterns designed by computer-

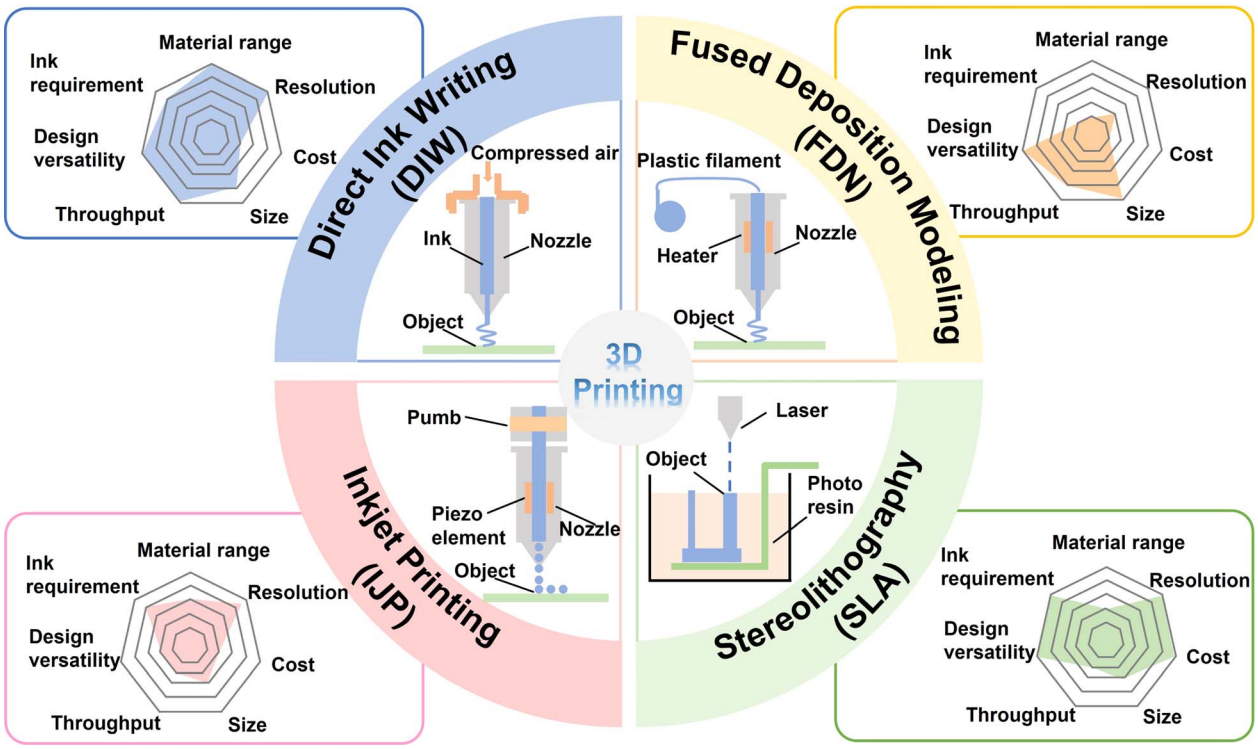

Fig. 2 Schematic of printing and characteristics of four representative 3D printing techniques (DIW, FDM, IJP and SLA) to fabricate MBs.

Table 1 Comparison of representative printing techniques

Method	Main materials	Resolution (μm)	Advantages	Disadvantage	Applications
DIW	Ceramic, plastics, metal composites	1–250	Material diversity, design versatility, 3D architectures	Additives, limited mechanical properties	LIMBs, NIMBs, ZIMBs, Li–S batteries; Li–O_2 batteries
FDM	Thermoplastics, glass, metals	50–200	Design versatility, high speed, simplicity	Weak mechanical Properties, limited materials	LIMBs
SLA	Photopolymers, UV-curable resins	10–25	Low cost, high resolution	Photosensitive additives, limited materials	LIMBs
SLS	Thermoplastics, metals, ceramics	80–250	Fine resolution, without support structure	Expensive, low efficiency	LIBs
IJP	Ceramics, metals, polymers	5–200	Low-temperature process, without support structure	Low surface quality	LIMBs, Zn–Ag MBs

aided design (CAD) software.[83] Following the deposition of each layer, the nozzle can smoothly move in a horizontal plane, and the platform can move vertically up and down, thereby producing desirable patterns with a tailored thickness and shape.[84,85] The resolution of the pattern can be synthetically determined by a combination of factors, including nozzle diameter, applied pressure, and ink features. It should be mentioned that the printability of ink is generally determined by its rheological properties, which is a key step towards the desired patterns.[86,87]

The rheological behavior of inks, including their viscosity, storage modulus (G') and loss modulus (G''), is intricately related to all their components.[88,89] Among them, viscosity is one of the most fundamental rheological parameters, describing the intermolecular interaction among the solvent, binder and particle surface.[90] The viscosity can be determined by a rotational test and plotted against shear rate, generating a characteristic flow curve.[91] According to the flow properties, inks can be divided into Newtonian fluid and non-Newtonian fluid, which represent a constant and variable viscosity at different shear rates, respectively.[92] To fulfill printability, the inks are required to be non-Newtonian fluids with shear-thinning behavior, which is also defined as pseudoplasticity and characterized by a decrease in viscosity with an increase in shear rate.[93] In addition, low-viscosity inks exhibit a droplet state, making them unsuitable for forming 3D structures, while extremely high-viscosity inks easily clog the nozzle, rendering them unprintable. Based on this, it is vital to form inks with an appropriate viscosity (10^3–10^5 Pa s at 0.01 s^{-1}) beneficial to the printing process. Beyond the required shear thinning

properties, the inks also possess viscoelasticity, where G' denotes the elastic behavior related to solid-like behavior and G'' represents viscous behavior indicative of inks with liquid-like properties.[94] Remarkably, the yield stress, denoting the intersection of G' and G'', serves as a critical rheological parameter, manifesting the transition between the solid-like and liquid-like states of inks. Specifically, under the yield point, G' is higher than G'', and the ink is more likely to maintain a solid-like shape.[95] Over the yield point, G'' exceeds G', presenting a dominant viscous feature, thus causing the ink to flow easily. This type of robust viscoelastic ink is favorable for precisely printing high-resolution customizable patterns.[96] Therefore, the synthesis of printable inks with suitable viscosity and yield stress behavior is critical to achieve the DIW printing process.

Among the representative printing techniques, DIW printing is the most widely used method in the manufacturing MBs, which is over 70% of 3D-printed MBs, owing to its particular features and superiorities. This technique has several noteworthy printing advantages, as follows: (1) a variety of printable materials, ranging from metals, ceramics, and polymers to carbon-based materials and nanomaterials, offering a multitude of possibilities for printable components for batteries;[45] (2) customizable shape, size and thickness, facilitating the easy construction of complex patterns and providing 3D-architecture versatility;[88] (3) high resolution, even reaching up to 1 μm;[97] (4) high throughput, especially having large-size printing ability by the use of multi-nozzle arrays;[98] and (5) high convenience of process procedures at low cost.[99] In fact, DIW printing has made significant strides in exploring high-performance 3D-printed active materials for MBs. It should be mentioned that the preparation of printable high-performance inks is still the main challenge associated with DIW for the fabrication of MBs.

Fused deposition modeling

FDM is one of the most extensively used modelling techniques and is another extrusion technique, in which thermoplastic materials are systematically deposited layer by layer onto a substrate by a heating process,[100] as illustrated in Fig. 2. In this method, thermoplastic materials are heated to the melting state, and then extruded from a nozzle, resulting in the ejection of semi-solid filaments. As the temperature drops, the materials solidify in a specific area, forming a single layer. Generally, a high melting temperature is beneficial to the strong adhesion between two adjacent extrusive filaments, further boosting the mechanical strength. Nevertheless, an excessive temperature will weaken the printed devices. Remarkably, the extrusion velocity has a significant effect on the melt morphology. Specifically, once the velocity goes beyond 20 mm s^{-1}, incomplete melting and interlayered cracks would be formed. If the velocity is less than 10 mm s^{-1}, a steady extrusion can occur. The finial structure depends on the melt viscosity, surface energy of substrate and drops, and the interaction between the nozzle and drop. Similar with the previously introduced 3D printing techniques, additional layers can be deposited on cured printing materials.[101] In some FDM printers, multiple squeezed nozzles can be used to deposit polymer components, especially for the construction of gradient components. Generally, the characteristics of the thermoplastic filament have a significant effect on the resolution and effectiveness of the patterns to a large extent. The main features of FDM are as follows: (1) the equipment is simple, low cost, and easy to operate; (2) the production process of "ejection-modelling" is convenient and almost no material waste is generated; (3) low heating temperature, no toxic gas and dust in the printing process; (4) low modelling accuracy, error and deformation prone; (5) low modelling rate, which is not suitable for the construction large devices. Compared with DIW, FDM printing exhibits limited material choice, and usually requires thermoplastic materials, such as polylactic acid, acrylonitrile butadiene styrene, polycarbonate, polystyrene, and polyamide. Furthermore, the above-mentioned thermoplastic materials with limited electrical conductivity were not used in MBs by FDM before 2016. To address the above-mentioned issues, several strategies have been developed, such as combination with carbon materials to enhance the conductivity of composites and depositing conductive substrates. However, FDM printing has a low resolution in the range of 50–200 μm and low throughput.[102] Different from DIW printing, which depends on printable inks, FDM is determined by the manufacturing of composite thermoplastic filaments.

Inkjet printing

IJP is one of the most common digital printing methods, which is a non-contact, non-mask and stress-free printing method.[103] This versatile technique has been used to print a variety of materials, including metals, ceramic, polymers and carbon-based materials. IJP has become a widely adopted manufacturing tool in many technical fields, including energy storage, electronics, integrated circuits, solar cells, sensors and photonic crystals.[64,104] Inkjet printers consist of a system controller, inkjet controller, nozzle, stage, *etc.* Under the control of the inkjet controller, the ink is sprayed on the target stage from the nozzle.[105] Generally, IJP processes can be divided into two categories, continuous IJP technology and drop-on-demand IJP (DOD-IJP) technology.[106] During the continuous IJP process, the nozzle constantly sprays the ink, and the superfluous ink is removed by the deflection device and recycling unit.[107]

The process of IJP can be divided into four steps including ink preparation, drop deposition, film formation and drying.[108] A vital step in the creation of high-resolution patterns is to prepare a stable and printable ink. The stability of an ink is determined by whether the functional materials are polymer-based or particle-based materials. Polymer-based inks require favorable compatibility between the solvent and polymer, in which chemicals with similar intermolecular forces tend to dissolve each other, which is called the "like dissolves like" principle. On the contrary, when the inks consist of particles, their stability is determined by the homogeneously distributed particles in the solvent. Stoke's law provides a quantifiable explanation for the stability of particle-based inks (eqn (1)), as follows:

$$v = \frac{2}{9}\frac{R_s^2(\rho_2 - \rho_1)g}{\eta} \quad (1)$$

where v denotes the settling velocity of particles, R_s represents the radius of the particle, ρ_2 and ρ_1 are the density of the particle and ink, respectively, g denotes the constant, and η represents the viscosity.[65] Remarkably, a stable ink requires the settling velocity to be as small as possible. According to eqn (1), a small particle radius, high viscosity and close density between particle and ink are more conducive to the formation of a stable ink. The stability of inks is independent of the printer character. It should be noted that there is a limitation in only adjusting a single parameter to increase the ink stability. For example, the viscosity value is not going to be infinite due to the limited viscosity range of the solvent, which should be suitable for printing. In the case of low-viscosity ink, the versatility of its structure design and the corresponding self-standing ability are limited, and hence the prepared patterns mostly tend to be presented in the form of thin films. Furthermore, the particle size cannot be reduced indefinitely, and high electrochemical activity should be considered when the particle size is reduced.

Similar to DIW printing, the printability in the IJP process depends on the fluid features, including dynamic viscosity, surface tension, and density. In the case of particle-type inks, their size distribution is a key factor in the printing process. The conditions of printable ink are usually described by the inverse of the Ohnesorge number (Oh), which is named the typical Z number and calculated using eqn (2), as follows:

$$Z = \frac{1}{\mathrm{Oh}} = \frac{\mathrm{Re}}{\sqrt{\mathrm{We}}} = \frac{(\gamma\rho\alpha)^{1/2}}{\eta} \quad (2)$$

where Re and We are the Reynolds and Weber numbers, respectively, γ represents the surface tension, ρ is the density, α denotes the diameter of the nozzle, and η represents the viscosity.[109] This equation adopting the ratio eliminates the velocity factor contained in Re and We and defines the printability of inks independent of the printer conditions.[110] Although the Z value is not strictly defined, it is generally accepted that this value of printable ink is between 1 and 14.[111] Moreover, most of the nozzles of IJP with a diameter in the tens of micrometers requires particle size of less than 200 nm to avoid clogging, in which small-size materials are favorable for high-resolution architectures. In addition, to avoid ink drying in the nozzle, the vapor pressure of the solvent should usually be less than that of water. Considering this, the introduced low-vapor-pressure solvents cause a challenge, where the residual solvents in the printed electrode or electrolyte layer may have an adverse impact on the electrochemical performance.[112]

Once the printable inks are formed, their droplets exhibit a characteristic shape when subjected to the descent process from the nozzle to substrate in the DOD-IJP technique. Firstly, the ink column is made thinner, forming the main droplet with a slender tail. The rupture of this tail will cause the formation of some small droplets that follow the main droplet, which are referred to as satellite droplets. If the flight distance between nozzle the and substrate is far enough, the satellite droplets usually merge with the main droplet. However, if they fall on the substrate as separate droplets, irregular patterns will be formed, which are harmful to deposition, resolution and accuracy. A wet layer of thin film is formed by overlapping adjacent droplets. The shape and size of the droplets are originally controlled by the impact force, and then controlled by capillary force. The uneven distribution of particles, that is, the "coffee ring effect",[113] is often observed in the drying of decentralized droplets, which is related on a variety of factors, including the substrate temperature, solvent composition and substrate/ink interaction. The coffee ring effect often occurs during the drying process. Thus, to avoid its formation, the evaporation of the solvent and the flow of the inks should be deliberately slowed down. In addition, several common post-treatments, such as high-temperature annealing, chemical and photon annealing and compression can form a well-defined printing pattern.

Stereolithography printing

SLA is a typical photocuring 3D printing method, which is also the earliest and most mature 3D printing technology.[114] In 1988, the first 3D printer based on photocuring was developed.[115] This technology has the advantages of high printing accuracy, fast printing speed, and good quality of printing objects. The core of SLA technology lies in the photosensitive resin.[116] During the printing process, an ultraviolet lamp emits a laser beam, irradiating on the photosensitive resin.[117] After shotting the above-mentioned resin slot by a laser beam, the molecular weight of the resin increases rapidly, and the liquid photosensitive resin transforms into the solid state. Once the one-layer resin is cured, the platform descends some distance and the next layer is cured again. This layer-by-layer approach continues until the desired 3D structure is produced. The completed device requires washing with appropriate solvents to remove the liquid remaining resin.

The materials used for SLA photocuring are different types of liquid photosensitive resins, and their components generally include matrix resin, diluent and photoinitiator.[118] These photosensitive resins usually have different mechanical and thermal properties, which depend on the selection of the matrix resins. The commonly used matrix resins include acrylic resin and epoxy acrylic resin. In the curing process, the acrylic photosensitive resin is a free radical photoinitiator, while the epoxy photosensitive resin is a cationic photoinitiator. Acrylic photosensitive resin corresponds to the free radical curing system. Under ultraviolet irradiation, the initiator molecule located at the ground state transitions to the excited state after absorbing light energy. The molecule in the excited state generates an active intermediate, which causes the polymerization of monomers to form a network of crosslinked structures. Epoxy photosensitive resin corresponds to the cationic curing system. During the illumination process, the photolysis of the initiator produces the strong Lewis-acid BF_3, which initiates polymerization with oxygen atoms containing lone pair electrons.[119] Free radical curing of acrylic photosensitive resin has the features of fast curing, high hardness, large brittleness, viscosity and volume change, which have an adverse effect on

the product accuracy.[120] Alternatively, epoxy-based photosensitive resin offers a low hardness and good flexibility, in which the epoxy bond in the epoxy resin is broken during curing, and then the bond length increases, which can make up for the shortcomings of volume shrinkage.[121]

Due to the unique working principle of the SLA technique, material selection is limited to meet the above-mentioned requirements. Remarkably, SLA can print high-resolution patterns with the minimum size down to 500 nm. Therefore, SLA is widely used in various applications ranging from flexible piezoelectric and dielectric sensors for health monitoring and human motion detection to aerospace, where the production of lightweight components is required with complex contours and high precision. Unlike the DIW, FDM and IJP printing technologies, SLA does not have the problem of nozzle clogging.[60] However, despite these advantages, its high cost and the trouble of addressing the sticky photopolymer hinder its industrial application. In addition, there may be other problems with the residual photoinitiator and uncured resin, causing impurities and toxicity.

Printable micro-battery components

The battery modules, including current collector/substrate, separator/electrolyte, cathode, anode and package, should be reasonably designed and fabricated, given that they have a vital influence on the performance of MBs, including their capacity, working voltage, energy density, power density, lifespan and safety.[122] In general, a single battery unit requires several specific characteristics, such as electrodes with both electrical and ionic conductivity, current collectors with electrical conductivity, electrolyte with ionic conductivity, and mechanical strength for accommodating volume changes.[123] Hence, it is necessary to use appropriate printing technology that is highly compatible with printable materials to satisfy the above-mentioned requirements, such as DIW for electrodes/electrolytes, FDM for substrates/current collectors, and SLA for packages. In this section, all the components of MBs prepared by 3D printing will be systematically summarized.

Universal methods to make materials printable

In brief, attempts have been made to make various battery materials to form inks, and the general methods for 3D-printable battery modules can be summarized based on various printing technologies. In the case of DIW and IJP technologies, the most important step is to prepare suitable inks for the follow-up printing process. Generally, the active materials are evenly mixed with binders, other additives and solvents in suitable ratios, forming printable inks with the desired viscosity and rheological behaviors to satisfy specific printing demands. In the preparation process, the physical and chemical properties of the active material and additives, such as surface functional groups, particle size, surface energy, polarity and viscosity, are strictly related to the formulation of the inks. In addition, to obtain an excellent pattern, the inks should have good wettability and adhesion to the substrate.

Compared with the DIW and IJP methods using printable inks, it is more difficult to prepare printable materials using FDM and SLA technologies. In the case of FDM printing, a raw material composite must be initially mixed with a thermoplastic matrix, and then extruded through an extruder, forming a filament with the appropriate size. Regarding SLA technology, desired curable inks consisting of active materials, polymer monomer and photoinitiators should be prepared in suitable proportions. Unfortunately, the direct printing of active materials *via* the SLA technique has not been reported. At present, certain battery components are indirectly built by printing templates *via* SLA technology. Overall, regardless of which 3D printing technology is chosen, systematic optimization, ranging from the choice of active material to the preparation of printable inks/filaments, is required for the creation of high-performance printed batteries.

Printing cathodes

The electrode is considered the most crucial component of MBs. Depending on its material, spatial configuration, and microstructure to printing technology, all aspects together determine the electrochemical performance of MBs. In this section, the latest research on 3D-printed cathodes for Li-ion batteries (LIBs),[124] sodium-ion batteries (NIBs),[125] Zn-ion batteries (ZIBs),[126] Li–S batteries,[127] Li–metal batteries (LMBs),[58] and Li–O_2 batteries[128] are summarized in detail.

Over the past few decades, several typical cathode materials have been printed for LIBs, such as $LiFePO_4$ (LFP),[129–133] $LiCoO_2$ (LCO),[134,135] $LiMn_2O_4$ (LMO),[136] $LiMn_{1-x}Fe_xPO_4$ (LMPF),[137] and $LiNi_{0.8}Co_{0.15}Al_{0.05}O_2$ (NCA).[138,139] Among them, LFP is the most popular printable cathode material,[140] which was printed using different technologies, such as DIW,[32,130–132,141,142] FDM,[78,143–146] and IJP.[147] For example, a flexible and compressible LFP cathode was printed through the DIW technique assisted by a directional freezing process (Fig. 4a).[124] This directional freeze-drying method could induce the vertical growth of ice crystals, further forming a vertical pore structure in the printed electrodes. Due to the intrinsic mechanical properties of the carbon nanotubes (CNTs) and cellulose nanofibers (CNFs), and the directional channels, it is a feasible precept to reach a balance between flexibility and high mass loading for 3D-printed thick electrodes. To further address the sluggish reaction kinetics, two-component conductive additives including acetylene black and CNTs were introduced to join LFP materials, forming continuous electron transfer channels.[131] In comparison to the conventional electrode by the slurry-casting method, the 3D electrodes achieved a trade-off between energy density and power density, endowing the thick electrodes with fast-charging capability. In addition, our group proposed the construction of 3D hierarchically conductive structures by adopting graphene, CNTs and acetylene black,[58] in which 0D acetylene black served the point of junction for adjacent LFP particles, 1D CNTs were uniformly distributed on the surface of the electrode material, while highly conductive graphene nanosheets provided 2D planar channels for electron transport, resulting in long-range ordered conductive networks. Consequently, the 3D-printed

LFP lattices showed an excellent areal capacity of 25.3 mA h cm^{-2}. Besides building fast electron pathways, it is important to reasonably design electrode materials. When the lithium intercalation becomes the rate-determining step, one effective strategy is to reduce the particle size to the nanometer-scale, shortening the ion diffusion path.[148] For example, Pan *et al.* prepared LMFP@C nanocrystals with an average particle size of ~40 nm for the fabrication of 3D-printed thick electrodes.[137] As shown in Fig. 4b and c, the 3D-printed LMFP@C showed superior capacity and outstanding rate capability with over 108 mA h g^{-1} even at an ultrahigh current density of 100 C. According to the theorical analysis (Fig. 4d), equivalent the ion diffusion coefficient was the determining factor in the rate performance of LIBs.

Compared with LIBs, NIBs are regarded as a class of promising power sources due to the abundant sodium resources and low cost. The cathode materials of NIBs, such as $Na_3V_2(PO_4)_3$ (NVP)[125] and $NaMnO_2$ (NMO),[149] were printed *via* the DIW and FDM methods. Unlike typical inks using polymer binders, graphene oxide (GO)-based inks only consisted of NVP particles and GO dispersions,[125] which had suitable rheological behaviors for DIW printing (Fig. 4e) due to the interaction between the solvent and surface functional groups of GO. The prepared skeleton was subjected to freeze-drying and annealing treatment to reduce GO (rGO), forming porous graphene-based conductive frameworks (Fig. 4f). Furthermore, complex structures including starfish, square/circle coils and circular crossing, could be viably achieved. Remarkably, the 3D-printed NVP-rGO cathodes exhibited an excellent performance for Na storage, showing a high areal capacity of 1.26 mA h cm^{-2} at 0.2 C, rate capacity with highly reversible capacity of 0.65 mA h cm^{-2} even at 20 C and exceptional stability with almost 90% initial capacity after 900 cycles at 1 C (Fig. 4g). In addition to the DIW technique, a freestanding NMO cathode based on a commercially available geometry by integrating active and supporting materials together, was achieved by FDM printing.[149] This provides a great paradigm for battery design towards next-generation energy storage systems and architecture.

Beyond alkali-ion batteries, multivalent-ion (*e.g.*, Zn^{2+}, Mg^{2+}, Ca^{2+}, and Al^{3+}) batteries have also been rapidly developed through 3D printing due to their high safety, eco-friendly nature and low cost. Particularly, ZIB cathodes were feasibly constructed by 3D printing. For instance, the printable ink consisting of $Fe_5V_{15}O_{39}(OH)_9 \cdot 9H_2O$ (FeVO) nanosheets and rGO had high viscosity and typical shear-thinning behaviors, which was successfully printed into different geometric shapes and various letter patterns on different substrates, such as glass, polyethylene terephthalate (PET), stainless steel and paper, demonstrating the versatility of DIW technology.[150] The 3D-printed FeVO-based cathodes exhibited a periodic macroporous structure composed of intersecting columns, providing rapid ion diffusion pathways. With an increase in the number of printed layers up to 4, corresponding to a mass loading of 24.4 mg cm^{-2}, the thick cathodes delivered a high areal capacity of 7.06 mA h cm^{-2}. In addition, Wu *et al.* reported the 3D-printing of a carbon-based lattice with modulable defects and periodic filaments, providing a favorable skeleton for the uniform deposition of MnO_2.[126] This prefect combination between 3D-printed frameworks and active materials regulated the homogeneous electric field distribution and enhanced the reaction kinetics. Consequently, the composite cathodes with a high mass loading of 28.4 mg cm^{-2} achieved an excellent areal capacity of 8.04 mA h cm^{-2}. This feasible combined strategy of 3D printing and subsequent deposition process was also demonstrated for the construction of a hierarchical core–shell structure. Pumera *et al.*[151] fabricated V_2O_5-deposited conductive carbon frameworks *via* FDM printing, in which the outer core of V_2O_5 provided high electrochemical activity, and the inner shell of the carbon framework offered long-range electron channels and interlinked ion diffusion networks. Remarkably, the printed V_2O_5 hybrid cathodes delivered a high specific capacity of 425 mA h g^{-1} at 0.3 A g^{-1} and fast-charging capability, exhibiting the excellent discharge capacity of 221 mA h g^{-1} at 4.8 A g^{-1}.

Recently, researchers have developed new printable battery systems with higher energy densities, such as Li–S batteries,[152–156] Li–Se batteries,[157] Li–O_2 batteries,[158] Na–O_2 batteries,[159] and Zn–air batteries.[160] For example, Yang *et al.* fabricated sulfur copolymer–graphene cathodes with periodic filaments *via* DIW printing.[161] The strong S–C bond in the cathode could partially inhibit the dissolution and shuttle effect of polysulfides, and the graphene matrix could enhance the conductivity of the whole electrode, thus improving the utilization of the active S material. Simultaneously, the 3D architecture could buffer the volume changes. Furthermore, Zhang group employed GO-based inks for printing a bracelet-like battery, delivering a specific capacity of 953 mA h g^{-1} under the sulfur mass loading of 10.2 mg cm^{-2}.[99] The low material utilization and sluggish reaction kinetics still enabled a high areal capacity in thick S cathodes with high mass loading. Here, Zhang *et al.* proposed an interfacial engineering approach by *in situ* decorating a 3D-printed carbonaceous scaffold with uniform surface-deposited Li_2S and healing the printed adjacent interface to eliminate the interfacial resistance.[162] Consequently, the 3D-printed Li_2S-based electrodes delivered an outstanding areal capacity and fast kinetics of 6.29 mA h cm^{-2} at 6 mA cm^{-2} under a high mass loading of 10 mg cm^{-2}. To address the ion transfer issue in thick electrodes, Sun *et al.* proposed dividing thick electrodes into vertically aligned 2D thin electrodes depending on ice walls (Fig. 5a).[163] The resulting sulfur cathodes had numerous macroscopic pores due to the arrange of filaments, improving the ion transport and electrolyte accommodation without changing the mass loading. Therefore, the electrodes with different layer thicknesses (250–750 μm) showed similar electrochemical performances with a specific capacity of about 1200 mA h g^{-1}.

Remarkably, GO ink can not only be used as a conductive substrate, but also as an active material for Li–O_2 batteries. A high-concentration holy GO ink (100 mg mL^{-1}) was prepared, which had suitable viscosity and typical shear-thinning properties, enabling smooth extrusion printing to produce multiple shapes.[128] The resulting printed electrodes exhibited hierarchical porous structures (Fig. 5b), including nanoscale holes on GO nanosheets and micro-level and millimeter-sized pores on

electrodes. The varying sizes of porosity in the 3D-printed GO-based lattices enriched the pathways for oxygen and electrolyte diffusion, further boosting the electrochemical performance of Li–O_2 batteries. Based on the idea of constructing porous structures, Wang *et al.* prepared hierarchically porous carbon networks derived from metal–organic framework (Co-MOF) ink through DIW printing (Fig. 5c).[158] There were abundant micro-sized pores within the derived carbon frameworks and meso- and micropores on the carbon flakes. The resultant hierarchical pore structures coupled with Co electrocatalysts were beneficial for the deposition of Li_2O_2 products and accelerating their conversion. Consequently, this reasonable Li–O_2 battery showed a high energy density of 798 W h kg^{-1} for the whole cell.

As shown in Fig. 3, it can be obviously seen that the printed cathode for LIBs occupied the maximum percentage of over 60%, followed by S-based cathodes. Form the viewpoint of technique, most cathodes were fabricated by DIW printing with a substantial proportion of over 70%. Considering the battery

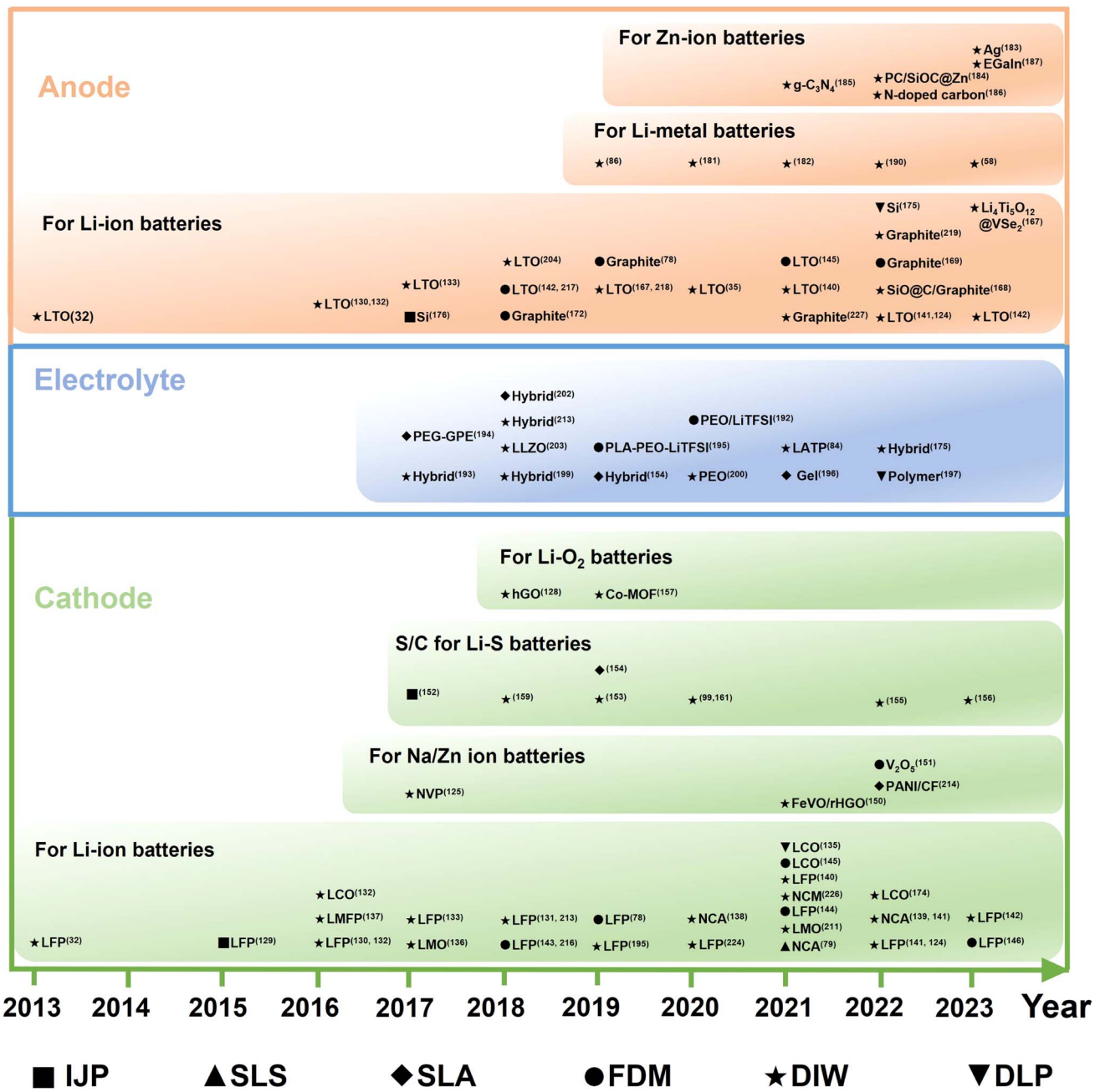

Fig. 3 Current representative 3D-printed cathodes, anodes, electrolytes *via* various printing methods. $LiFePO_4$ (LFP), $LiCoO_2$ (LCO), $LiMn_2O_4$ (LMO), $LiMn_{1-x}Fe_xPO_4$ (LMFP), $LiNi_{0.8}Co_{0.15}Al_{0.05}O_2$ (NCA), $LiNi_{06}Co_{0.2}Mn_{0.2}O_2$ (NCM), $Na_3V_2(PO_4)_3$ (NVP), $NaMnO_2$ (NMO), sulfur and carbon (S/C), poly(ethylene glycol) (PEG), $Li_7La_3Zr_2O_{12}$ (LLZO), $Li_4Ti_5O_{12}$ (LTO), and polyaniline (PANI)-coated carbon fiber (PANI/CF).

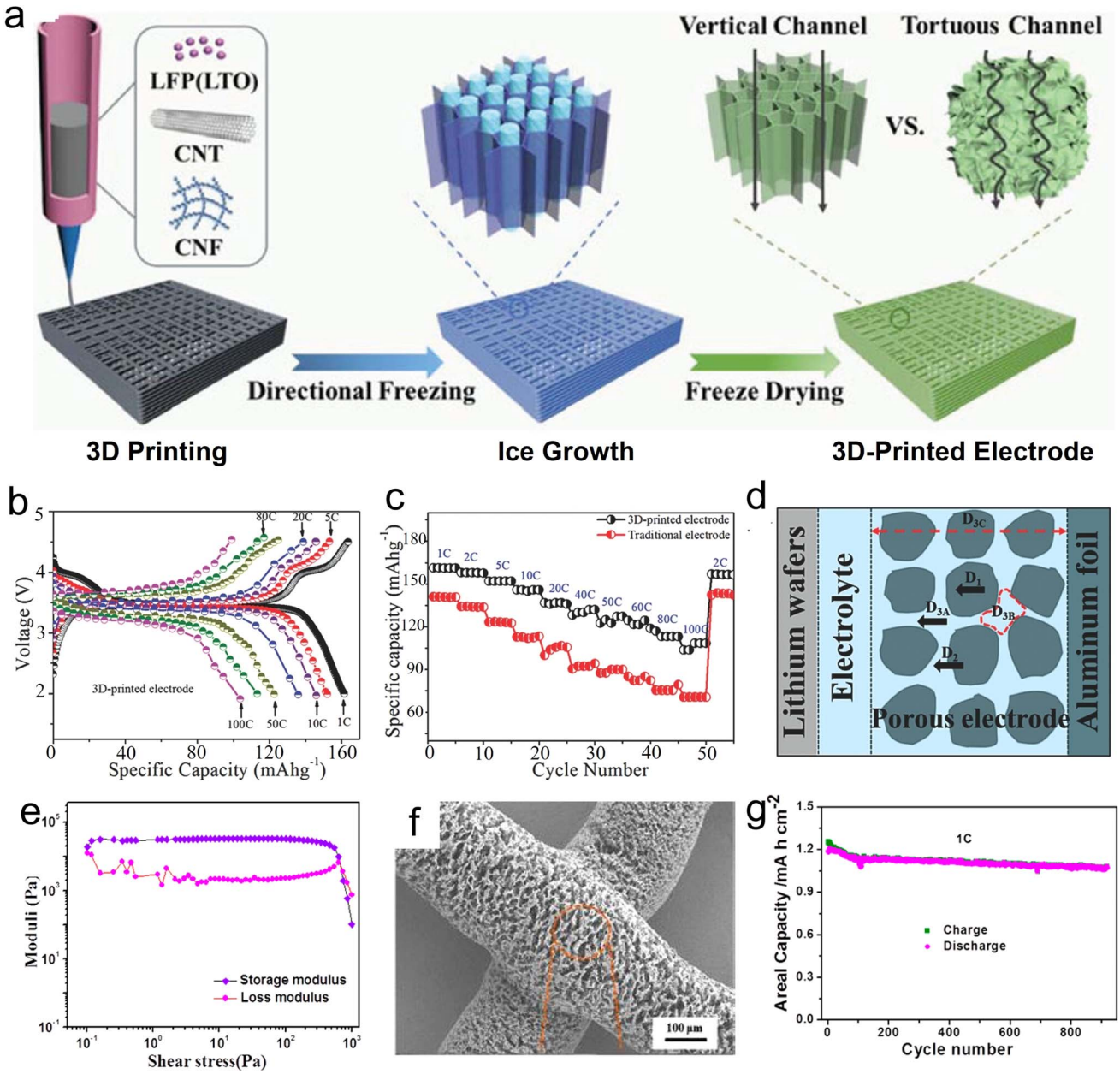

Fig. 4 3D-printed cathodes for LIBs and NIBs. (a) Schematic of 3D-printed LFP cathodes by DIW technique (3DP electrode: 3D-printed electrode). Reproduced from ref. 124. Copyright 2022, Wiley-VCH. (b) Galvanostatic charge–discharging profiles, (c) rate capability and (d) Li-ion transport in 3D-printed LMFP@C cathodes. Reproduced from ref. 137. Copyright 2016, Wiley-VCH. (e) G' and G'' of NVP inks. (f) SEM image of 3D-printed NVP cathodes. (g) Cycling performance of 3D-printed NVP cathodes tested at 1 C. Reproduced from ref. 125. Copyright 2017, The American Chemical Society.

system, it can be expected that a continuous increase towards advanced next-generation high-energy batteries will occur.

Printing anodes

Thus far, the most popularly printed anode is $Li_4Ti_5O_{12}$ (LTO) *via* DIW printing,[164,165] owing to its various advantages of zero strain and high reversibility during lithium intercalation/de-intercalation process. For example, Liang *et al.* prepared 3D conductive LTO anodes with 1D Ag nanowires, 2D GO nanosheets and LTO nanoparticles together as printable inks (Fig. 6a).[166] The printed thick electrodes exhibited an open mesh configuration with abundant micropores, promoting the penetration of the electrolyte. Both Ag nanowires and graphene nanosheets served as a conductive bridge for the LTO particles, offering long-range and rapid electron transfer channels. Besides, the 2D graphene nanosheets with excellent flexibility are supposed to enhance the integral stability of thick electrodes. As a result, the elaborate thick LTO anodes with the thickness of 1500 μm delivered a high areal capacity of 4.74 mA h cm^{-2} and excellent cycling stability due to their

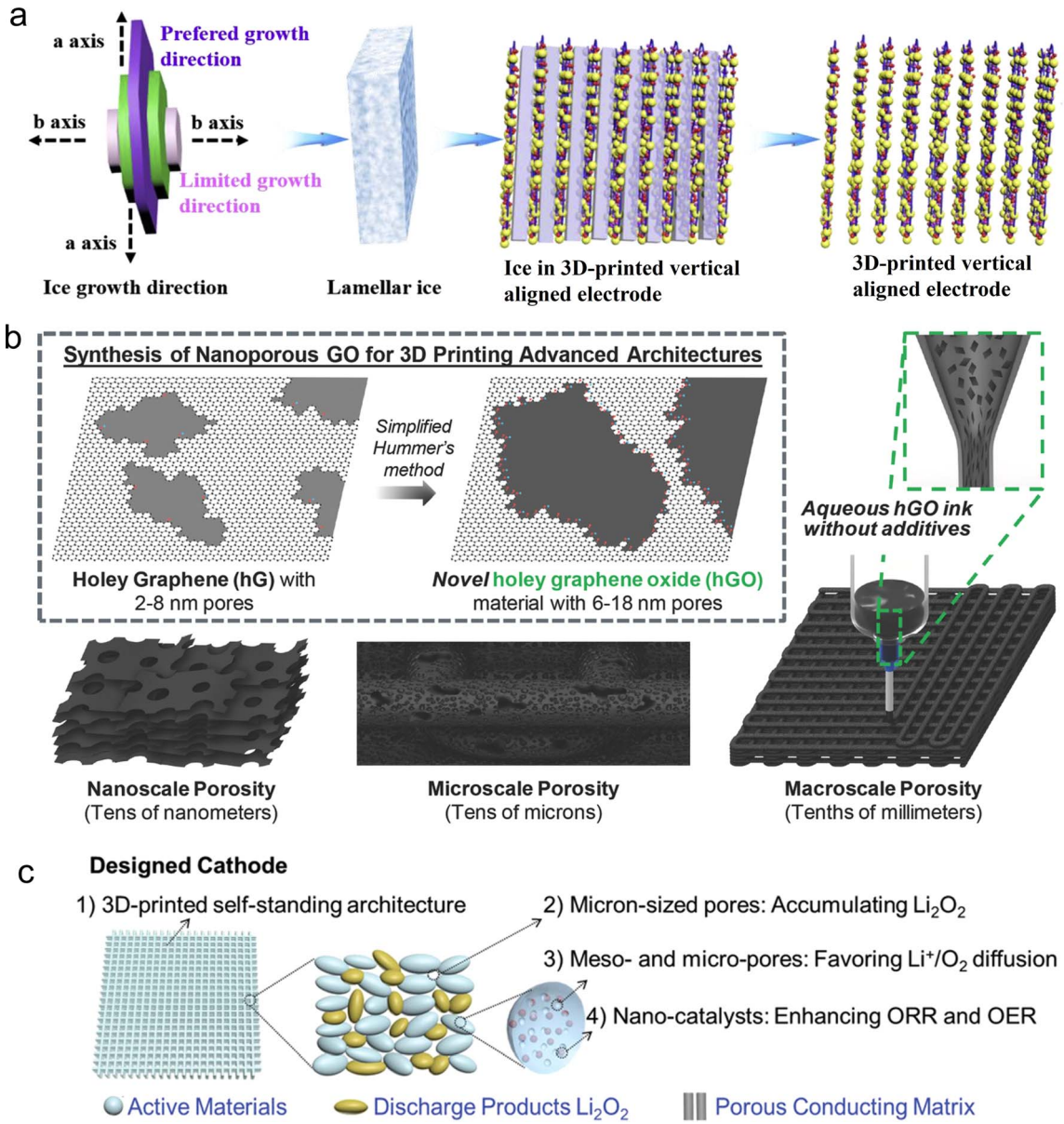

Fig. 5 3D-printed cathodes for Li–S batteries and Li–O_2 batteries. (a) Schematic of growth mechanism of thin electrodes by ice template. Reproduced from ref. 163. Copyright 2020, Elsevier. (b) 3D-printed GO electrodes with hierarchical porous structures for Li–O_2 batteries. Reproduced from ref. 128. Copyright 2018, Wiley-VCH. (c) Schematic of 3D-printed hierarchically porous carbon networks accelerating the deposition and conversion of Li_2O_2 for Li–O_2 batteries. Reproduced from ref. 158. Copyright 2019, Wiley-VCH.

hierarchically conductive networks, boosting the electron and ion transport (Fig. 6b). In terms of electrode materials, Liu *et al.* constructed printable LTO@VSe_2 composite materials to enhance the stability, capacity contribution and reaction kinetics, as follows: (1) the coated VSe_2 layer served as a barrier, avoiding direct contact with the electrolyte and improving the interfacial stability and (2) the LTO@VSe_2 heterostructure shortened the diffusion distance of ions and improved the electrochemical activity.[167] Consequently, the 3D-printed LTO@VSe_2 anodes delivered a remarkable rate capability with a specific capacity of 128 mA h g^{-1} at 10 C.

Furthermore, other printable anode materials with a higher theoretical specific capacity have been developed, such as graphite,[168,169] SnO_2,[170] ZnSe,[171] and silicon (Si).[172] For example, Dupant *et al.* reported the preparation of a 3D-printed graphite anode *via* the FDM method, delivering a reversible capacity of 200 mA h g^{-1} at 18.6 mA g^{-1} (Fig. 6c).[173] Due to the good printability of the prepared inks composed of graphite, polylactic acid and plasticizer, the printed filaments with mechanical strength were assembled into a complex 3D architecture, such as high-solution semi-cube framework and boat-like skeleton. Utilizing a similar method, lithium-terephthalate (Li_2TP) anodes were printed with Li_2TP/polylactic acid inks *via* the FDM technique.[174] These works provide a novel way to construct versatile 3D structures towards next-generation MBs *via* FDM. To satisfy the demand of stretchable devices,

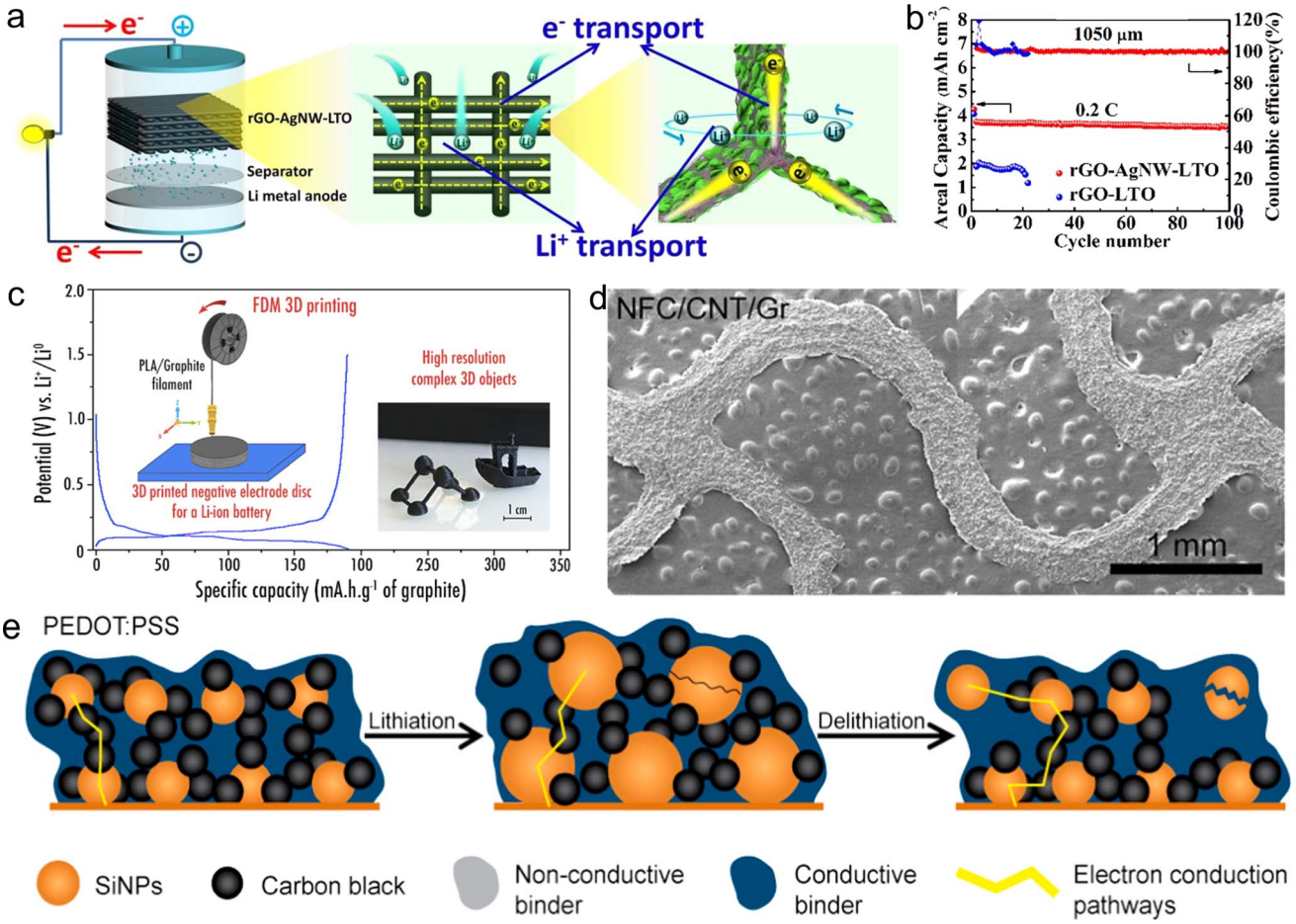

Fig. 6 3D-printed anodes for LIBs. (a) Schematic of 3D-printed LTO inks composed of Ag nanowires, GO nanosheets and LTO nanoparticles as anodes enhancing the ion/electron transport in LIBs and (b) corresponding cycling performance at 0.2 C. Reproduced from ref. 166. Copyright 2020, Elsevier. (c) Galvanostatic charge–discharge (GCD) profiles and photograph of 3D-printed graphite anodes *via* FDM method. Reproduced from ref. 173. Copyright 2018, The American Chemical Society. (d) SEM image of 3D-printed serpentine graphite anodes *via* DIW printing. Reproduced from ref. 175. Copyright 2022, Elsevier. (e) Schematic illustration of the enhanced electrochemical performance mechanism of 3D-printed anodes with PEDOT:PSS additive. Reproduced from ref. 176. Copyright 2017, Elsevier.

a graphite-based ink with active material, CNTs and CNF was used to print serpentine lattices *via* the DIW method (Fig. 6d),[175] where the serpentine structure enabled excellent deformability by buffering the strain, and the robust interactions between CNTs and CNF enhanced the mechanical flexibility. The 3D-printed graphite anode delivered a high specific capacity, suggesting the presence of numerous conductive channels and high electrochemical activity of graphite in the 3D-printed thick anodes.

Si is regarded as a candidate material to replace graphite anodes for LIBs due to its higher theoretical specific capacity (4200 mA h g^{-1}). For instance, Ye *et al.* proposed the fabrication of a honeycomb-network Si/poly(3,4-ethylenedioxythiophene)-poly(styrene sulfonate) (PEDOT:PSS)/PEG anode by DLP method,[172] in which the pore size was controllable from the macro to micro scale. Besides, a large number of uniform structures with tight packaging and high-resolution patterns could be manufactured rapidly. Due to the well-designed microscale matrix and the introduction of PEDOT:PSS conductive additive, the printed patterns provided long-range conductive channels for insulating the Si nanoparticles, and further increased the discharge capacity. To deeply understand the enhancement mechanism of PEDOT:PSS for Si anodes, Sun *et al.* fabricated different Si anodes using four types of binders *via* the IJP technique, such as PEDOT:PSS, polyvinylpyrrolidone (PVP), carboxymethyl cellulose (CMC) and Na-alginate.[176] Remarkably, PEDOT:PSS not only bound the electrode structure due to its self-healing property, but also was uniformly coated on the Si nanoparticles, accelerating rapid electron transfer (Fig. 6e). Compared with CMC- and PVP-based Si electrodes with only point-contact and line-contact between conductive additives and Si nanoparticles, the printed PEDOT:PSS-based Si anodes with 3D conductive channels greatly enhanced the reversible lithiation/delithiation process.

Similarly to the 3D-printed cathodes of NIBs and ZIBs, the corresponding anodes have also been developed, such as MoS_2 [177] and Cu_2S@ZnS/C.[178] A printable aqueous ink incorporating MoS_2 and GO nanosheets was used to fabricate an

aerogel by the IJP method and freeze-drying process, resulting in high-precision patterns with adjustable microstructure and macroscopic architectures.[177] The printed MoS_2/rGO hybrid as anodes for NIBs showed a high reversible specific capacity of 429 mA h g^{-1}. To increase the electron and ionic transfer kinetics at the material level, Zhang *et al.* designed Cu_2S@ZnS/C heterostructure nanohybrids with abundant defects and uniform carbon coating layer.[178] This elaborate heterostructure is beneficial to enhance the electrochemical activity and boost the reaction kinetics, providing a high reversible capacity and rate capability for Na ion storage.

Recently, more efforts have been focused on next-generation high-energy printable metal anodes, such as Li,[179–182] Na and Zn,[183–187] due to their high theoretical capacity and lower redox potential. In general, it is critical to reasonably design framework architectures to buffer the volume changes and suppress dendrite formation, exhibiting the following combined traits: (i) a porous 3D conductive scaffold to hold a vast deposition amount and buffer the huge volume expansion of metal; (ii) large specific surface area to availably homogenize the local current distribution; and (iii) massive lithiophilic sites to effectively regulate the ion flux.[181,188–190] Our group fabricated 3D porous MXene lattices by using high-concentration MXene ink (300 mg mL^{-1}), regulating the lithium nucleation behavior and homogenizing lithium deposition (Fig. 7a–c).[58] The outstanding lithiophilic properties of the $Ti_3C_2T_x$ MXene could regulate the nucleation of metallic Li, forming a homogeneous LiF-enriched solid-electrolyte interphase layer and stabilizing the interface of Li/electrolyte. Consequently, the $Ti_3C_2T_x$ MXene electrodes synchronously realized an excellent rate capacity, ultrahigh Li stripping/plating capacity of 80 mA h cm^{-2} at 4 mA cm^{-2} and exceptional lifespan of over 4800 h. In addition, hydrogel-like

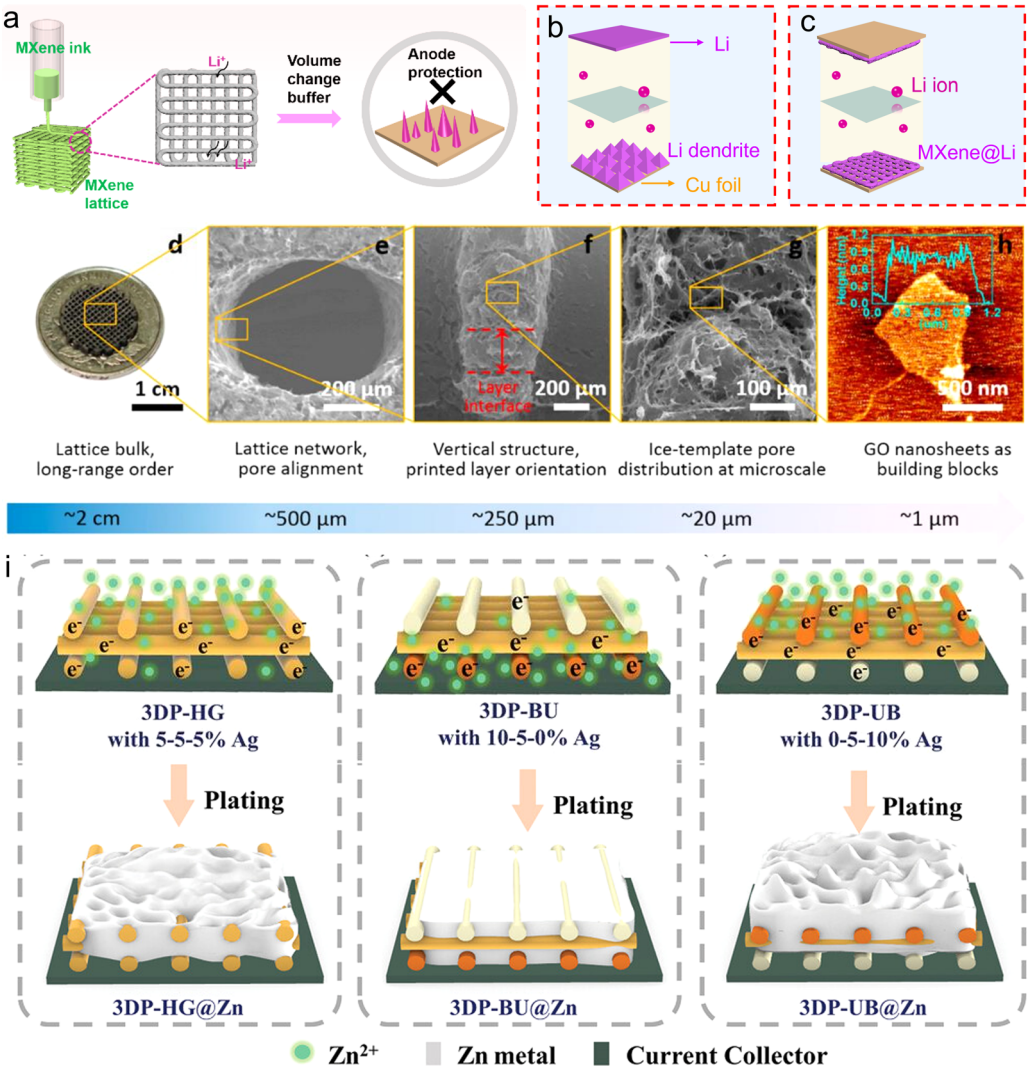

Fig. 7 3D-printed conductive frameworks for stable metal anodes (Li, Na, Zn). (a–c) Schematic of 3D-printed MXene lattices suppressing dendrite growth and volume changes in Li metal. Reproduced from ref. 58. Copyright 2023, Elsevier. (d–h) SEM images of 3D-printed GO frameworks showing hierarchical structure on multiple scales. Reproduced from ref. 191. Copyright 2019, The American Chemical Society. (i) Schematic illustration of 3D-printed gradient-structure Ag lattices for protecting Zn anodes. Reproduced from ref. 183. Copyright 2023, Wiley-VCH.

lattices were constructed using GO inks by DIW printing.[191] The resulted super-elastic graphene lattice exhibited hierarchical structures with a length on the micrometer to millimeter scale. In the vertical direction, the adjacent filaments formed a compact and seamless interface, ensuring well-established electron pathways (Fig. 7d–h). Consequently, the printed graphene lattice could effectively regulate the Na deposition, thus showing a long lifespan of 1000 h and high coulombic efficiency of 99.84%. Further, an *in situ* artificial inorganic SEI layer, consisting of Li_2S and Li_3N in the 3D-printed sulfur and nitrogen-doped GO films, was reported to address the dendrite growth issues and alleviate lithium-metal volume expansion.[192] These results open a novel way to rationally design 2D materials towards high-stability metal anodes. To investigate the structure–performance relationship, Zhang *et al.* fabricated layer-by-layer carbon frameworks with a gradient Ag content.[183] The Ag nanoparticles located at different positions exhibited varying electron transfer capabilities, resulting in gradient electron flux from the top layer to the bottom layer (Fig. 7i). Due to the high binding energy between Ag and Zn, the Ag nanoparticles concentrated at the bottom would induce more Zn ions towards the bottom of the electrode. The 3D-printed frameworks with bottom-up declining Ag nanoparticles could construct dual-gradient electron/ion fluxes, enabling smooth electron/ion transfer in the electrode. Similar to printed cathodes, the DIW technique occupies a dominant position in all printed anodes.

Printing electrolytes

In general, liquid or gel electrolytes are commonly used for 3D-printed electrodes, which cannot be printed for LIBs, NIBs, ZIBs and Li–S batteries.[44] Recently, printable electrolytes, such as inorganic ceramic,[84] polymer[193] and inorganic-polymer composites,[194] have been prepared towards solid-state batteries, due to their high thermal and chemical stability, thus preventing the common flammability and leakage issues when using liquid electrolytes.[195] Importantly, the printable solid-state electrolytes also served as separators, enabling the compatible integration of all-printed batteries.[196] Nevertheless, less attention has been focused on electrolyte printing in comparison to electrodes.

Gel electrolytes can be categorized as aqueous, organic, and ionic liquid gel electrolytes according to their different conductive components in the solvent, which are bound to the host polymer substrates such as polyvinyl alcohol (PVA), polymethyl methacrylate (PMMA), and poly(vinylidene fluoride-*co*-hexafluoropropylene) (PVDF-HFP).[197] Aqueous gel polymer electrolyte has high ionic conductivity and low cost, making it widely used in printable MBs. Unfortunately, its narrow stable electrochemical window and the printer nozzle corrosion caused by strong acid or strong alkali limit its application.[53] Thus, in the search for high-voltage electrolytes, an organic gel polymer electrolyte consisting of salts (*e.g.*, $LiPF_6$, lithium bis(-trifluoromethanesulphonyl)imide (LiTFSI), and $NaClO_4$) and organic solvents (*e.g.*, ethylene carbonate (EC), propylene carbonate (PC), and dimethyl carbonate (DMC)) was developed, achieving a broad voltage window beyond 3.5 V.[198] As an alternative to aqueous and organic gel polymer electrolytes, ionic liquid gel electrolyte has good mechanical stability and nonflammability in addition to a high voltage window.

Remarkably, a ceramic–polymer hybrid electrolyte exhibited enhanced mechanical stability, printability and electrochemical properties by introducing inorganic fillers (*e.g.*, Al_2O_3 and SiO_2) in a gel polymer electrolyte.[199] For example, Shahbazian-Yassar *et al.* fabricated a hybrid solid-state electrolyte ink with PVDF-HFP gel networks, Pyr_{13}TFSI ionic liquid, LiTFSI salt, and TiO_2 filler, which could be smoothly printed onto the electrodes by the DIW technique, greatly improving the fabrication efficiency of the whole device (Fig. 8a).[200] Besides, this polymer-based electrolyte could be printed on complex-structured substrates, such as hemisphere, allowing the fabrication of arbitrary-shape batteries. As an important component of ink, TiO_2 nanoparticles were used to regulate the rheological property and the contact angle, enabling good interfacial contact between the electrodes and electrolytes, and thus reducing the interfacial resistance. As a result, the optimized electrolyte ink realized an excellent ionic conductivity of 0.78 mS cm^{-1} due to the Lewis acid–base interactions between the TiO_2 fillers and the polymer networks. More importantly, the printed 3D-structured electrolytes by the DLP method were conducive to shortening the ion diffusion distance, strengthening the interface contact between the electrolyte and electrodes, and increasing the mass loading of materials in comparison to the traditional electrolyte (Fig. 8b).[201] Lee *et al.* proposed an ultraviolet (UV) curing-assisted printing strategy for the fabrication of bipolar flexible LIBs,[202] in which the printed gel composite electrolytes enabled the creation of MBs with various form factors. Therefore, the all-printed LIBs showed excellent flexibility and nonflammability, extremely exceeding that with inorganic electrolytes.

In addition to the above-mentioned gel polymer-based electrolytes for quasi-solid-state batteries, 3D-printed ceramic electrolytes have also been developed.[203] Bruce *et al.* fabricated different-structure hybrid electrolytes with cubic, gyroidal, diamond and spinodal shapes through a 3D printing template and further filling $Li_{1.4}Al_{0.4}Ge_{1.6}(PO_4)_3$ (LAGP) and epoxy (Fig. 9a).[204] The microstructures of 3D electrolytes could be accurately regulated by the ratio between the ceramic and polymer, which are strictly related with the electrical and mechanical properties. Consequently, a 3D ordered bi-continuous ceramic–polymer hybrid electrolyte was achieved, exhibiting high ionic conductivity of 0.16 mS cm^{-1} and exceptional mechanical properties. Furthermore, Hu *et al.* designed a flexible composite electrolyte membrane composed of garnet $Li_{6.75}La_3Zr_{1.75}Ta_{0.25}O_{12}$ (LLZO) and styrene-butadiene copolymer using DIW printing, simultaneously achieving good electrochemical performance and mechanical flexibility.[205] To minimize the interfacial resistance between the electrolyte and electrode, Hu *et al.* constructed a self-supporting LLZO ink,[203] which was printed into different structures with a high aspect ratio, including line, grid and column (Fig. 9b). The 3D-printed LLZO electrolyte with a continuous layer-by-layer structure enhanced the ionic conductivity and suppressed the growth of lithium dendrites.

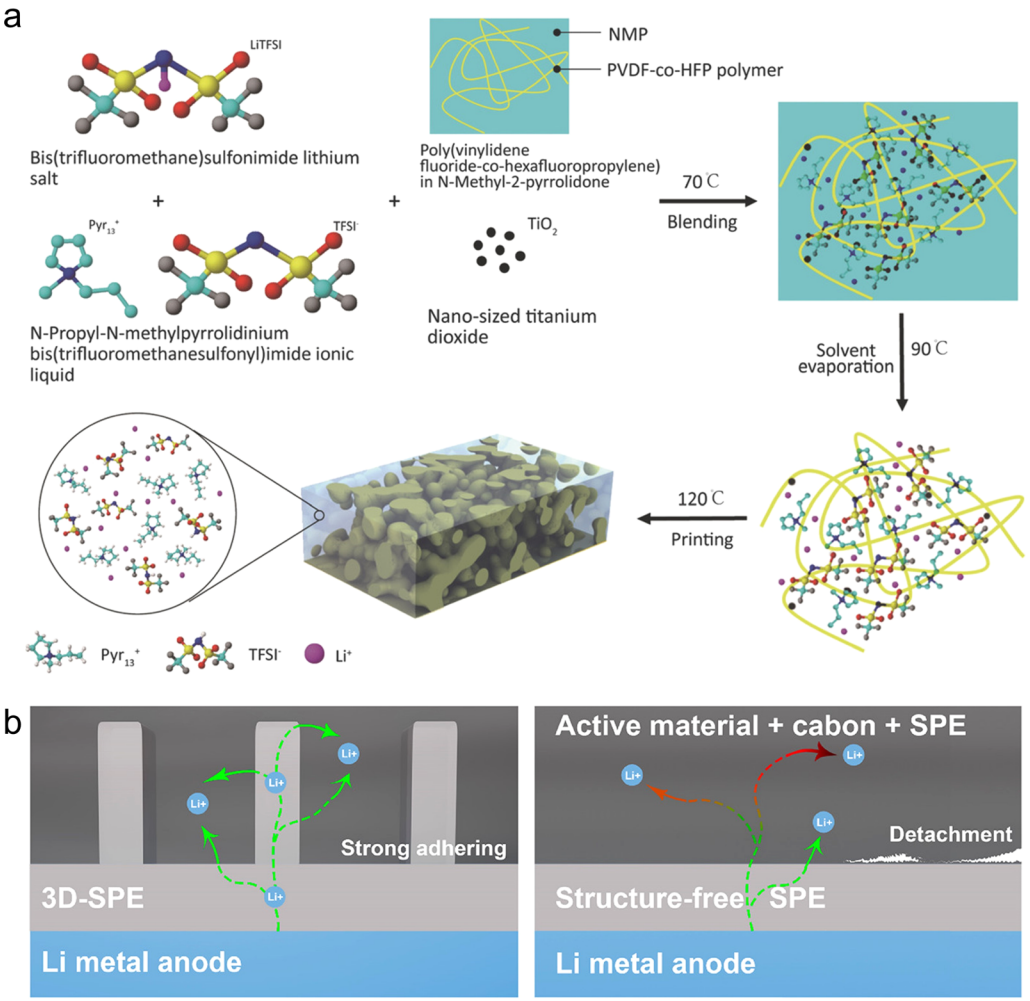

Fig. 8 3D-printed hybrid-based solid-state electrolytes. (a) Schematic illustration of the composition and preparation process of 3D-printed $Pyr_{13}TFSI$-based electrolyte inks. Reproduced from ref. 199 Copyright 2018, Wiley-VCH. (b) Schematic of 3D-printed and structure-free electrolytes *via* SLP method (SPE: solid polymer electrolyte). Reproduced from ref. 200. Copyright 2020, The American Chemical Society.

Printing current collectors and substrates

In addition to electrodes and electrolytes, other elements, such as current collectors, separators and packages, can be assembled into tunable configurations by 3D printing techniques using relevant inks/filaments. Current collectors play a role in supporting the electrodes and connecting them with external circuits, especially when the electrode lacks sufficient conductivity to carry electrons, enabling electrochemical reactions for MBs. Regarding the substrate, it is an important non-active component, serving as a support material for a current collector or an electrode. Considering the innate advantages of metal materials as current collectors, the SLS and SLM techniques have become important for the fabrication of current collectors. IJP is also a popular method for printing current collectors and substrates due to its ability to prepare thinner films. It should be noted that the DIW technique can also be used because of its low cost and high resolution. Otherwise, polymer substrates or frameworks can be achieved by FDM and SLA printing, improving the electrical conductivity through filling metal or conductive carbon-based materials.

Metals are conventionally used as current collectors, such as stainless steel, Cu, Ti, Au, Al and Ni.[44] Nevertheless, extreme printing scenarios for manufacturing metal-based current collectors are usually required using transitional printing techniques. In addition, the printed metal-based current collectors are stiff and heavy, making them incompatible with flexible MBs and easy to undergo mechanical deformation, causing the separation of the electrode materials and current collectors as the electrochemical progress, which further exerts a negative impact on the lifespan and energy density of MBs.[15,206] Considering this, carbon-based materials, especially graphene and CNTs, are widely used as current collectors due to their high electrical conductivity, stability, lightness and good mechanical features.[207]

In comparison to classical stacked-configuration current collectors, developing novel-structure current collectors (substrates) exhibiting diversiform configurations is favorable for accelerating ion/electron transfer by increasing the effective contact area between the electrode materials and electrolytes, thus enhancing the electrochemical performance of MBs.[12] For example, double-spiral current collectors and electrode-

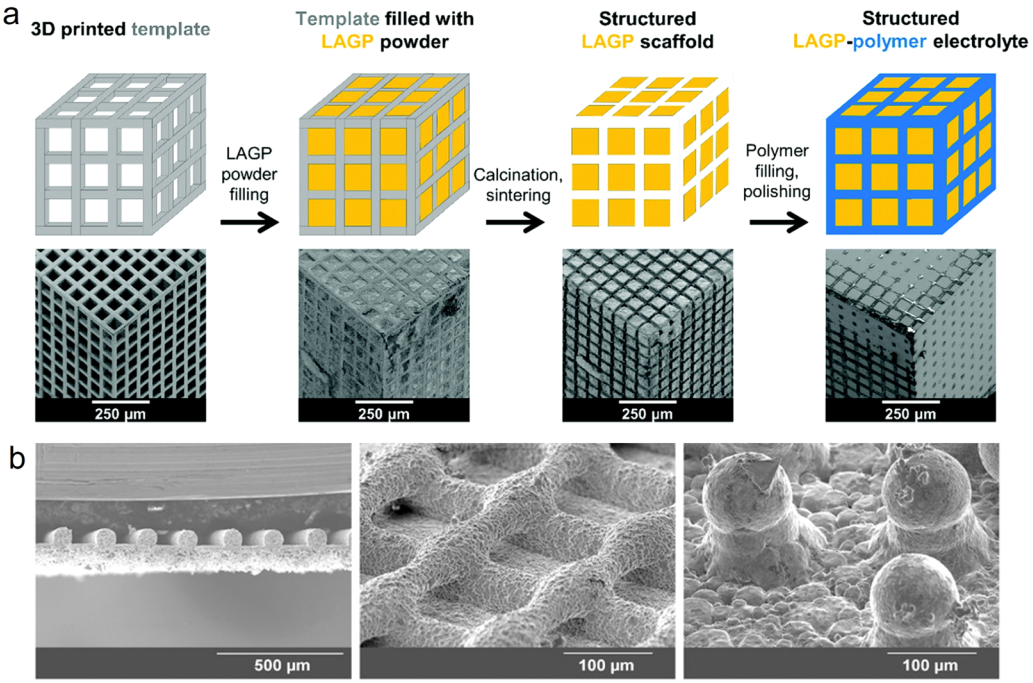

Fig. 9 3D-printed ceramic-based solid-state electrolytes. (a) Schematic illustration of the preparation process of 3D-printed LAGP electrolytes. Reproduced from ref. 203. Copyright 2018, The Royal Society of Chemistry. (b) SEM images of 3D-printed LLZO electrolytes at different magnifications. Reproduced from ref. 202. Copyright 2018, Wiley-VCH.

integrated composites were achieved by FDM printing (Fig. 10a).[143] The internal current collectors and the external LTO anodes could be simultaneously printed. Consequently, the morphology of the 3D-printed LTO anode was very smooth, and the LTO particles and polymer were evenly distributed in the printed electrodes.

In the case of the substrate, it needs to possess crucial physicochemical properties, including flexibility, surface flatness, stability, and strong adhesion to the electrodes or current collectors. According to previous reports, there are common substrate materials, such as polymers (PET, PDMS), metal foils (Cu, Zn, Al, and Ti), silicon wafers, wood, glass and paper.[9] Nevertheless, the 3D-printing of substrates is still in the initial stage, which has not been widely implemented. As an example, the SLA technique was employed to directly print porous high-conductivity metal substrates, which could be used not only to support the electrodes but also avoid the use of current collectors.[208] However, the inevitable post-processing involves lengthy steps and significant time requirement, restricting the further development of 3D-printed metal-based substrates. As a substitute, polymer substrates with high flexibility and thermostability can be printed. For instance, polymer-derived ceramics were used to print a rigid 3D SiOC scaffold, where the rigid ceramic materials are favorable for boosting the structural stability. Their well-organized 3D porous structure can induce rapid ion migration along the vertical channels in the electrodes and enhance the contact between the electrode and electrolyte (Fig. 10b).[209] Interestingly, adjusting the size of the 3D electrodes can regulate their local current density and the distribution of zinc ion concentration, leading to a higher electrochemical performance. This work provided insight for a good explanation of the structure–performance relationship. In addition, a specially designed 3D-printed polymer lattice

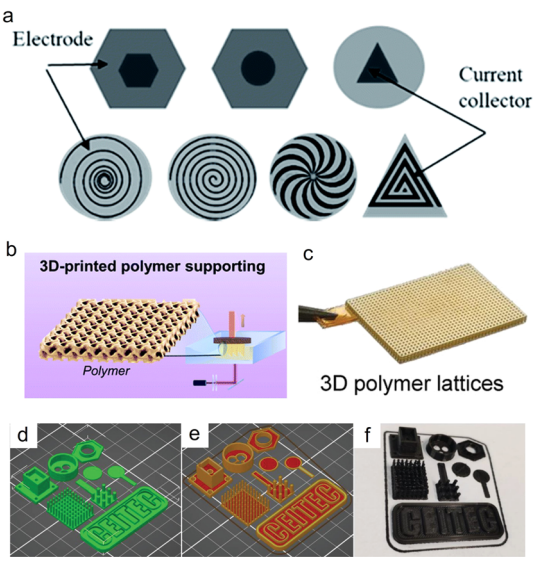

Fig. 10 3D-printed current collectors and substrates. (a) Schematic of 3D-printed double-spiral current collectors and electrodes. Reproduced from ref. 143. Copyright 2018, The Royal Society of Chemistry. (b) Schematic of 3D-printed polymer-derived ceramics substrates. Reproduced from ref. 208. Copyright 2022, The Royal Society of Chemistry. (c) 3D-printed polymer lattice for substrate. Reproduced from ref. 57. Copyright 2021, Wiley-VCH. (d and e) Schematic and (f) photograph of 3D-printed different patterns and sizes of substrates by FDM printing. Reproduced from ref. 211. Copyright 2021, Wiley-VCH.

achieved a high printing resolution of up to 10 μm (Fig. 10c).[57] Prior to metallization, the fabricated polymer lattice underwent oxygen plasma treatment and $KMnO_4$ solution immersion to enhance the wettability of the 3D-printed lattice. Remarkably, the polymer lattice exhibited a multi-channel structure and could effectively regulate the electric field distribution, further realizing homogeneous Zn deposition.

Novel substrates with high stretchability and various configurations can significantly boost the design versatility and accommodate the arbitrary shape of desired devices. Lee *et al.* used the DIW method to construct stretchable substrates based on PDMS polymer resin.[210] To overcome the soft viscoelasticity of printed soft silicone resin, ultrafine sugar particles were added to the PDMS elastomer, obtaining the ideal viscosity for the uniform printing process. Besides adjusting the rheological behavior of compatible PDMS inks for smooth DIW printing, ultrafine sugar particles play a significant role in introducing abundant porosity in the stretchable substrates. The battery materials could be loaded into the printed porous substrates, allowing the formation of stretchable electrodes. The above-mentioned results certify the possibility of the 3D printing strategy to construct stretchable electrodes, which may provide inspiration for wearable electronics using a 3D-printed stretchable power supply. Furthermore, polymer substrates with various shapes and 3D perforated structures were printed, such as cylinders, plates and cubes.[211] The 3D conductive polymer substrates with mutually perpendicular through-holes had a higher surface area than silicon substrates. As a result, the fabricated MBs on polymer substrates delivered a superior areal energy density compared to the silicon-based MBs. In addition, the patterns and sizes of the substrates can be easily adjusted by FDM printing (Fig. 10d–f).[212] By changing the printed thickness, it is possible to endow the printed substrates and electrodes with good mechanical flexibility. Thereby, this advanced strategy offers new opportunities, especially for the customizable manufacturing of flexible microelectronics with complex graphics.

Printing separators

Different from the current collectors requiring ionic insulation and high electrical conductivity, the separators act as continuous channels for ions and insulators for electrons, which are placed between the cathodes and anodes, avoiding the short circuit. Various separator patterns can be easily realized by 3D printing.[78] Hu *et al.* printed a separator based on BN with good thermal stability and electrical insulation properties by the DIW technique (Fig. 11a), as well as providing thermal management in LMBs, NIBs, Li–S batteries and Li–O_2 batteries.[213] The printable inks consisted of BN nanosheets and PVDF-HFP, which could produce a uniform separator composed of spiral patterns, providing continuous Li-ion transport pathways and great heat-distributed interface. Also, the printed adjacent filaments were connected to each other, finally forming a complete film with a thickness in the range of 20 to 100 μm. During the Li stripping/plating process, the 3D-printed BN-separator is conducive to rapid thermal dispersion, thus improving the safety and cyclability of the batteries. This study offered an

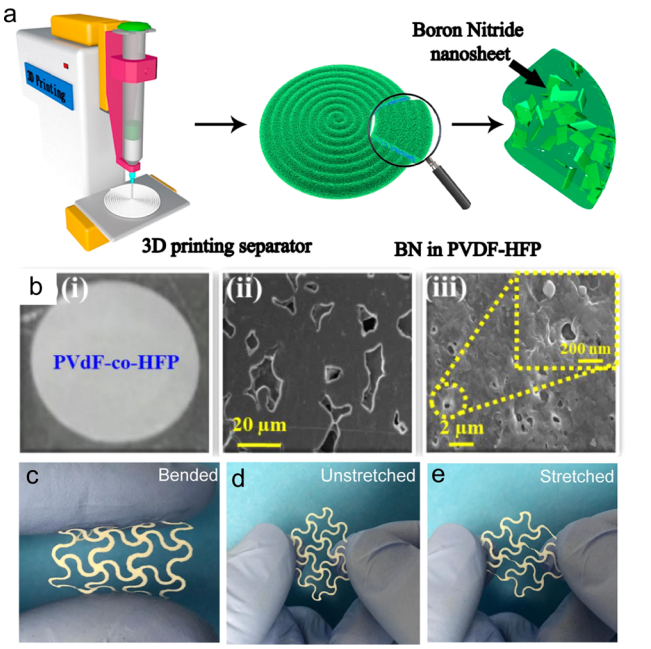

Fig. 11 3D-printed separators. (a) Schematic of the 3D-printed BN separators. Reproduced from ref. 213. Copyright 2018, Elsevier. (b) Photograph (i) and SEM images (ii and iii) of 3D-printed PVDF-HFP separators. Reproduced from ref. 138. Copyright 2020, Elsevier. (c–e) Photographs of 3D-printed bendable and stretchable NFC/Al_2O_3 separators. Reproduced from ref. 175. Copyright 2022, Elsevier.

effective strategy for the manufacture of thermal management partitions for LMBs. In addition, PVDF-HFP inks were prepared and printed into a separator for energy storage devices (Fig. 11b).[138] Compared to the commercial Celgard 2320 separator, the printed separator with less porosity but faster electrolyte absorption could achieve higher ionic conductivity and faster wettability. Furthermore, the printed PVDF-HFP-based separators showed good mechanical stability and high abuse resistance, which played a crucial role in ensuring the safety of the battery. In addition to printed separators, NCA cathodes and graphite anodes were also printed. As a result, the all-printed pouch cells delivered a high capacity of 187 mA h g^{-1} and excellent mechanical flexibility under adverse bending conditions. These high-performance LIBs with design versatility and excellent flexibility by 3D printing technology provide opportunities for power supply in wearable electronics.

Not only flexible devices, but highly stretchable batteries are also required for microelectronics and smart sensors. In this regard, the electrodes and separator must endure repeated stretching and maintain their structural integrity for supporting a steady operation. For instance, Li *et al.* proposed a 3D-printing strategy using nanofibrillated cellulose (NFC) to fabricate stretchable LIBs.[175] A serpentine separator was printed using NFC/Al_2O_3 ink, where Al_2O_3 could enhance the ionic conductivity of the separator and promote the uptake of the electrolyte, and NFC was helpful for improving the mechanical properties (Fig. 11c–e). Consequently, the printed NFC/Al_2O_3 separators achieved a high tensile strength and Li^+ transference number of

0.56, demonstrating excellent mechanical properties and electrochemical performance.

Printing packages

The package is a crucial component of MBs, which greatly affects their electrochemical performance. Although the package is not an electrochemically active material, it protects the electrode and electrolyte and avoids the leakage of the electrolyte. Thus, well-designed packages guarantee favorable sealing and protect from air and water. Generally, the packages and sealants are made of adhesives and heat-sealing polymeric materials. Notably, the 3D-printed package that encapsulates all units of MBs is a simplified and cost-effective process to construct fully printed MBs, and even on-chip integration towards practical applications. In addition, 3D-printed packages can form good binding with the encapsulated electrodes/electrolytes/current collectors/substrates, dispersing the stress/strain in the charging-discharge process, and further boosting the electrochemical and mechanical performance.

3D-printed packaged LIMBs were achieved based on printed cathodes, anodes, electrolytes and packages by the DIW technique (Fig. 12a).[214] The packaging ink consisted of fumed SiO_2 particles and UV-curable epoxy. As shown in the preparation process of MBs, the anode inks were extruded onto the cured package wall. To finish the complete battery manufacturing, the packaging ink was deposited onto the top of cathodes, realizing good bonding and sealing. The resultant packages provided a protective barrier for the electrolytes and electrodes, ensuring multi-functional integration for microelectronics. In addition, SLA technology was used to manufacture ring, cylinder and H-shaped polymer packages (Fig. 12b–d).[215] These packages could effectively encapsulate the as-fabricated cathodes, anodes and separators. Consequently, fully packaged customizable ZIMBs were constructed by sealing epoxy resin. In addition to the DIW and SLA methods, FDM printing has been widely used in the fabrication of printed packages. For instance, Pan *et al.* designed conformal PVDF-based packages with planar and non-planar structures for customizable LIBs *via* FDM printing (Fig. 12e and f).[216] It should be mentioned that the printing parameters (*e.g.*, printing speed) can be reasonably adjusted based on the requirements of the sealed packages to produce various structures with inherent characteristics. Remarkably, the enclosures could be printed into specific shapes for compatible integration with other microelectronic devices

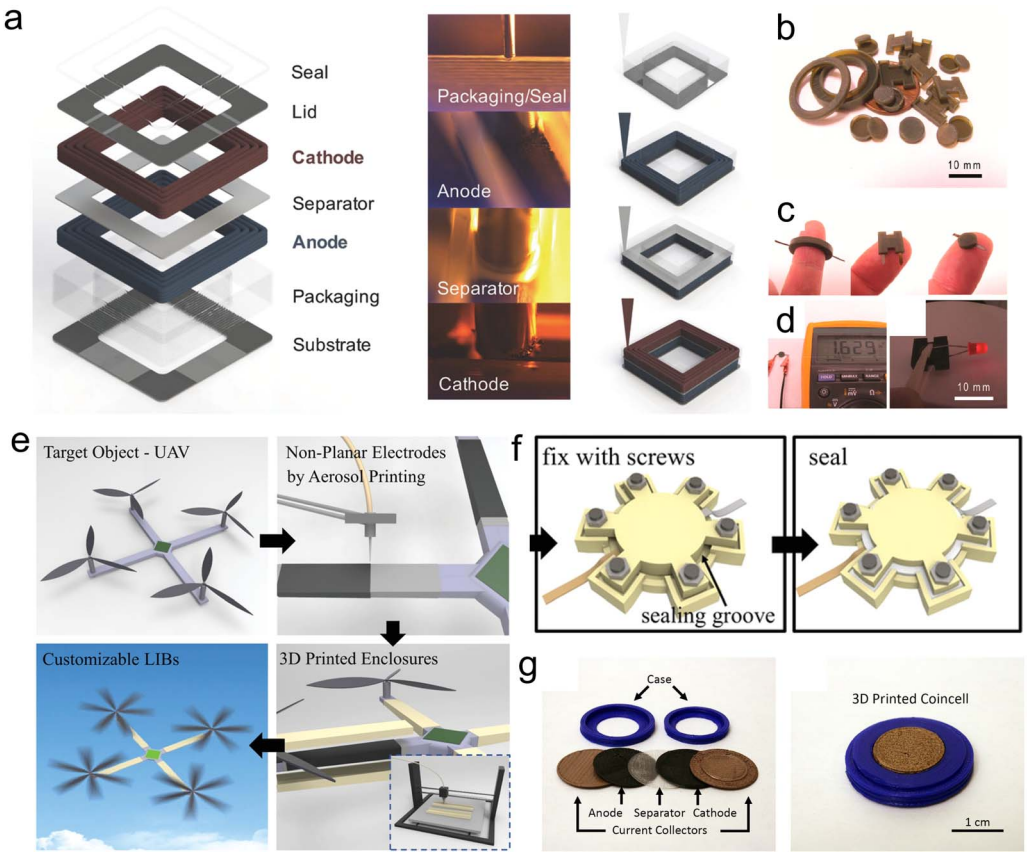

Fig. 12 3D-printed packages. (a) Schematic of the components of 3D-printed LIBs. Reproduced from ref. 214. Copyright 2018, Wiley-VCH. Photographs of 3D-printed different-shape packages (b) and Zn-PANI batteries (c). (d) Photographs of LED powered by 3D-printed packaged Zn-PANI battery. Reproduced from ref. 215. Copyright 2018, The American Chemical Society. (e and f) Schematic of the fabrication process of 3D-printed planar LIBs. Reproduced from ref. 216. Copyright 2019, Wiley-VCH. (g) Photographs of 3D printed coin cell. Reproduced from ref. 217. Copyright 2018, The American Chemical Society.

(Fig. 12g).[217] These results provide ideas to create printable materials and devices, which can be designed into arbitrarily shaped MBs.

3D-printed micro-battery

Next, recent advances in 3D-printed MBs will be summarized according to the charge carrier in electrolytes, such as LIMB,[218,219] NIMB,[33] and ZIMB.[13] As shown in the development milestones of printable batteries (Fig. 13), the first prototype of 3D-printed MB was fabricated by the IJP method,[220] with Zn as the anode and Ag as the cathode. Afterwards, 3D-printed planar/fiber-shaped LIMBs were designed *via* DIW technology.[32,130,133] From 2018, the development of novel printable battery systems substantially increased, such as Li–O_2 batteries,[128] Zn–air batteries,[221] Li–S batteries,[161] K–Se batteries,[222] ZIMBs and NIMBs.[33,215] Also, the representative reports on 3D-printed MBs in recent years are summarized in Table 2.

3D-printed Li-ion micro-battery

Over the past few decades, LIBs have been extensively researched and commercialized due to their high energy density and long cycle life.[223] In recent years, new manufacturing methods of MBs with arbitrary structure and good electrochemical properties have been continuously explored.[19,224] Lewis *et al.* pioneeringly constructed a prototype of an interdigital LIMB using the DIW technique, which consisted of an LFP cathode and LTO anode (Fig. 14a).[32] Due to the exceptional rheological behavior of the as-prepared inks, the printed multiple-layer microelectrodes showed a high aspect ratio, achieving a high resolution even at thick electrodes (Fig. 14b). It should be mentioned that the packaged LIMBs tested in liquid electrolyte delivered a decent areal capacity of 1.2 mA h cm^{-2} (Fig. 14c). Despite the lack of effective encapsulation strategies to achieve long-term cycling stability, this work provided a blueprint to fabricate printable and packaged LIMBs for next-generation microelectronics. Afterwards, Hu *et al.* employed GO-based electrode inks to construct 3D-printed interdigital LIMBs

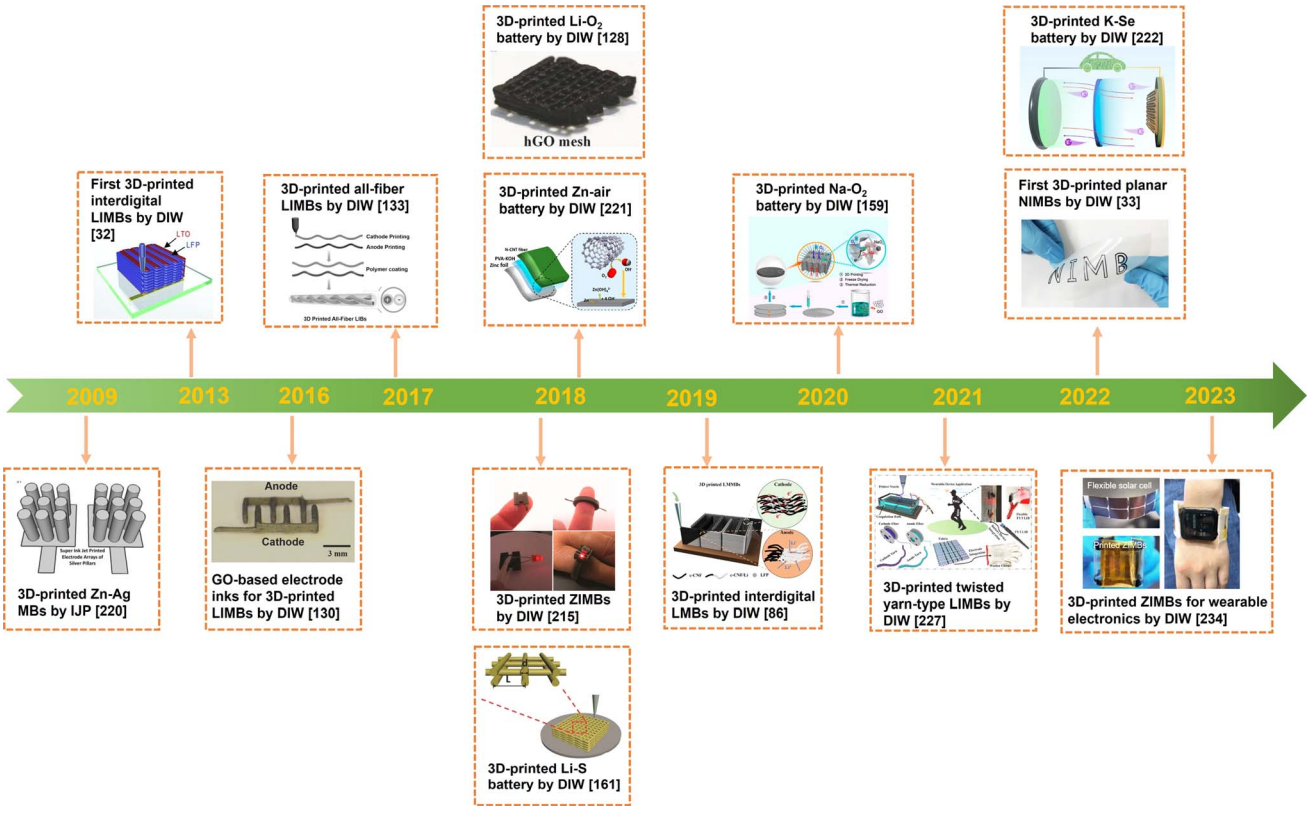

Fig. 13 Timeline of the development of 3D-printed various MBs. Inset images: "3D-printed Zn–Ag micro-battery by IJP". Reproduced from ref. 220. Copyright 2009, IOP Publishing. "3D-printed interdigital LIBs by DIW". Reproduced from ref. 32. Copyright 2013, Wiley-VCH. "3D-printed GO-based electrode inks for LIBs by DIW". Reproduced from ref. 130. Copyright 2016, Wiley-VCH. "3D-printed all-fiber LIBs by DIW". Reproduced from ref. 133. Copyright 2017, Wiley-VCH. "3D-printed Li–O_2 battery by DIW". Reproduced from ref. 128. Copyright 2018, Wiley-VCH. "3D-printed Zn–air battery by DIW". Reproduced from ref. 221. Copyright 2018, The American Chemical Society. "3D-printed ZIMBs by DIW". Reproduced from ref. 215. Copyright 2018, The American Chemical Society. "3D-printed Li–S battery by DIW". Reproduced from ref. 161. Copyright 2018, Wiley-VCH. "3D-printed interdigital LMBs by DIW". Reproduced from ref. 86. Copyright 2019, Wiley-VCH. "3D-printed Na–O_2 battery by DIW". Reproduced from ref. 159. Copyright 2020, The American Chemical Society. "3D-printed twisted yarn-type LIBs by DIW". Reproduced from ref. 227. Copyright 2021, Elsevier. "3D-printed planar NIMBs by DIW". Reproduced from ref. 33. Copyright 2022, Wiley-VCH. "3D-printed K–Se battery by DIW". Reproduced from ref. 222. Copyright 2022, The American Chemical Society. "3D-printed ZIMBs for wearable electronics by DIW". Reproduced from ref. 234. Copyright 2023, The Royal Society of Chemistry.

Table 2 The electrochemical performance of 3D-printed MBs

Device	Material	Method	Configuration	Electrolyte	Voltage (V)	Flexibility	Capacity	Energy density	Power density	Ref.
LIMB	LFP//LTO	DIW	Interdigital	$LiClO_4$-EC/DMC	1.0–2.5	—	1.2 mA h cm^{-2}	9.7 J cm^{-2}	2.7 mW cm^{-2}	32
	LFP//LTO	DIW	Interdigital	$LiPF_6$-EC/DEC	1.0–2.5	—	1.64 mA h cm^{-2}	—	—	130
	LFP//LTO	DIW	Serpentine	$LiPF_6$-EC/DEC	1.0–2.5	—	130 mA h g^{-1}	—	—	225
	LFP//LTO	DIW	Fiber	$LiPF_6$-EC/DEC-PVDF-HFP	1.0–2.5	—	110 mA h g^{-1}	—	—	133
	NCM622//graphite	DIW	Fiber	$LiPF_6$-EC/DEC-PVDF-HFP	2.7–4.3	—	2.3 mA h cm^{-2} 162 mA h g^{-1}	—	—	227
NIMB	NVPF//NTP	DIW	Interdigital	$NaBF_4$-EMIMBF$_4$-PVDF-HFP	0.8–2.6	Capacity retention of 93% (180°)	4.5 mA h cm^{-2}	7.33 mW h cm^{-2}	29 mW cm^{-2}	33
	NVP//NVP	DIW	Fiber	$NaClO_4$-EC/PC/FEC	1.0–3.0	—	50 mA h g^{-1}	—	—	228
ZIMB	Zn//MnO_2	—	Interdigital	2 M $ZnSO_4$ 0.1 M $MnSO_4$	0.9–1.8	Capacity retention of 96.3% (180°)	304 μA h cm^{-2}	168 μW h cm^{-2}	4.5 mW cm^{-2}	232
	CaVO//rGO@Zn	DIW	Interdigital	$Zn(CF_3SO_3)_2$-PVA	0.3–1.4	—	14.9 mA h cm^{-2}	—	—	233
	V_2O_5//Zn	DIW	Interdigital	$Zn(CF_3SO_3)_2$	0.2–1.8	Flexible	10.1 mA h cm^{-2}	8.1 mW h cm^{-2}	—	234

(Fig. 14d).[130] Remarkably, the GO nanosheets played significant roles, as follows: (i) highly concentrated GO with adjustable viscoelastic and rheological properties enabled the smooth printability of the electrode inks, (ii) GO after annealing treatment possessed high electrical conductivity, boosting the electron transfer kinetics in the 3D-printed thick electrodes, and (iii) the GO-based electrode inks without any binders enhanced the content and utilization of the electrochemical active materials. The printed interdigital LIMB arrays exhibited satisfactory uniformity and layer-by-layer structure, reaching up to 18 layers, corresponding to the thickness of 3.26 mm. As a result, the 3D-printed GO-based LIMBs delivered a specific capacity of 91 mA h g^{-1} at 50 mA g^{-1} (Fig. 14e and f). To cater for the growing interests in flexible and stretchable devices, Li *et al.* fabricated viscous inks with electrode materials of LFP and LTO, conductive additive of CNTs and PVDF binder for the construction of serpentine-structured electrodes *via* the DIW method (Fig. 14g).[225] According to the finite element analysis and electrochemical measurements, the well-designed serpentine-shaped electrodes could buffer strain when subjected to deformation condition, strengthening their mechanical stability. As a result, the assembled pouch cell showed an excellent capacity of 120 mA h g^{-1} and could power an LED with unchanged brightness in the bent, twisted, and folded states. These 3D-printed LIMBs with elaborate structure design provide a deep insight into the construction of flexible high-energy power sources towards wearable microelectronics.

Compared with interdigital-shape LIMBs, 1D fiber-based LIMBs are more compatible with flexible, foldable and substrate-free microelectronics. To pattern fiber-type structures in a fast and scalable way, Hu *et al.* employed the DIW method to fabricate all-fiber-based LIMBs consisting of an LTO anode, LFP cathode and PVDF-HFP-based gel polymer electrolyte (Fig. 15a).[133] The electrode inks (LFP and LTO) were extruded into ethanol solution in a coagulation bath to prepare continuous and high-flexibility fibers. Remarkably, a long LFP fiber of almost 23 cm with good mechanical strength was obtained, having the ability to lift weight. The as-fabricated all-fiber twisted LIMBs were tested in polymer electrolyte, delivering a high specific capacity of 110 mA h g^{-1} at 50 mA g^{-1}, and good flexibility, powering a LED without failure under the bending state (Fig. 15b). Moreover, the 3D-printed fiber electrodes could be knitted into fabric (Fig. 15c), indicating their widespread application in wearable microelectronics. To reduce the content of binder in the electrode inks for improving the conductivity and mass loading of electrodes, a feasible *in situ* interface reinforcement strategy was proposed to construct binder-free fiber-based LIMBs (Fig. 15d) by printing GO-based electrode inks into a coagulating bath consisting of dopamine (DA) and $CaCl_2$.[226] Remarkably, the polymerization process of polydopamine (PDA) with the catalyzation of Ca^{2+} built strong crosslinks between the LFP nanoparticles and GO nanosheets and enhanced the interface networks. Furthermore, the PDA-derived carbon could produce π–π interactions with rGO nanosheets and form a robust bond with LFP materials, delivering a high capacity of 146 mA h g^{-1} (Fig. 15e). This elaborate design of inks coupled with the reinforcement effect was beneficial to obtain high-flexibility and high-durability 3D-printed fiber electrodes in a large-scale architecture (Fig. 15f). To

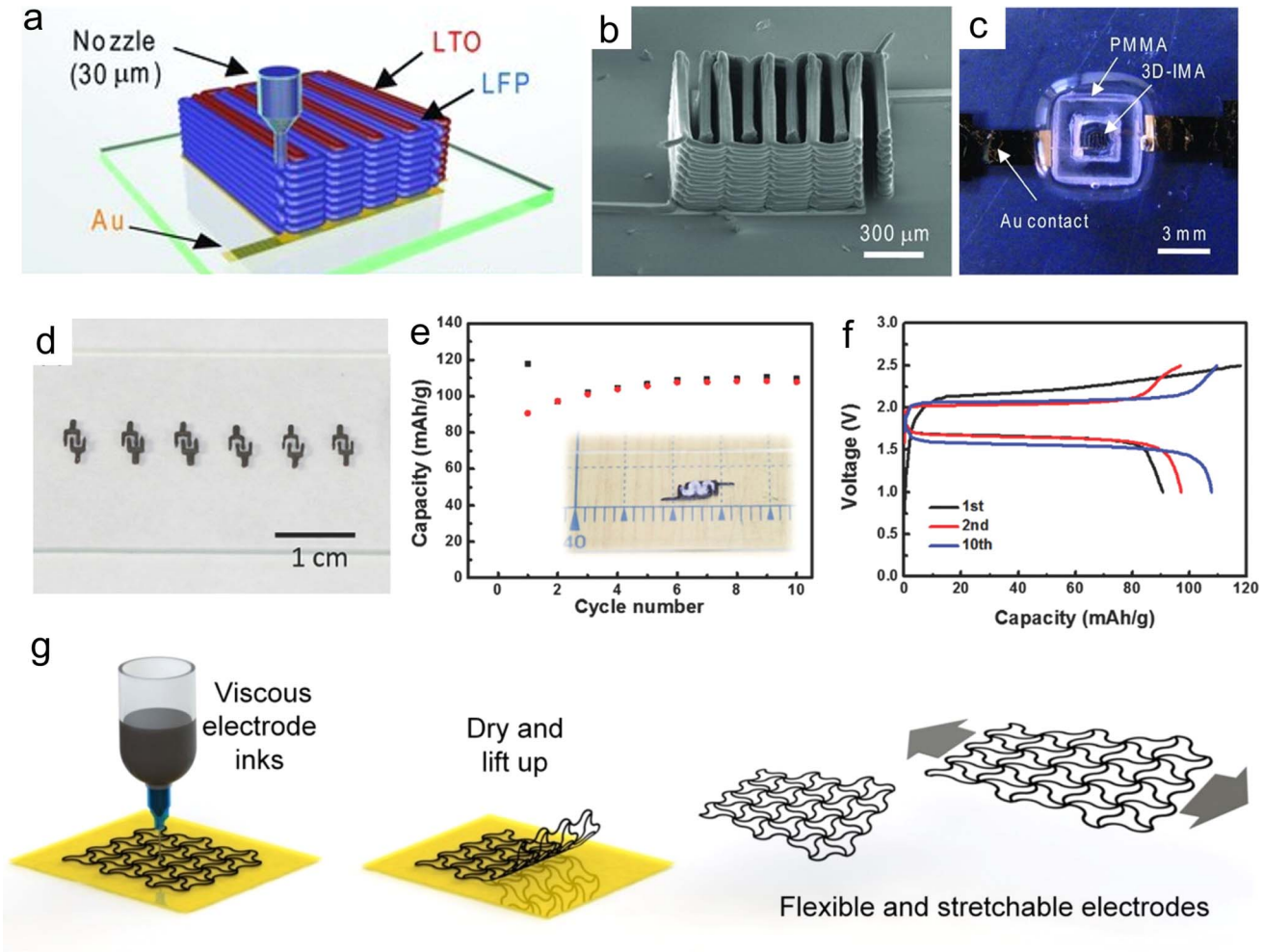

Fig. 14 3D-printed planar LIMBs. (a) Schematic illustration of 3D-printed interdigital LIMBs on Au current collectors. (b) SEM image of 3D-printed interdigital microelectrodes. (c) Photograph of the packaged LIMBs by PMMA. Reproduced from ref. 32. Copyright 2013, Wiley-VCH. (d) Photograph of 3D-printed GO-based microelectrodes. (e and f) Cycling performance and corresponding GCD profiles of 3D-printed LIMBs, respectively. Reproduced from ref. 130. Copyright 2016, Wiley-VCH. (g) Schematic illustration of the fabrication process of 3D-printed stretchable electrodes. Reproduced from ref. 225. Copyright 2020, Elsevier.

demonstrate the application of the fiber-based LIMBs in smart wearable devices, a prototype of twisted yarn-type LIB with NCM811 cathode and graphite anode by DIW printing was integrated with smart fabrics (Fig. 15g and h), delivering a highly reversible specific capacity of 166 mA h g^{-1}, corresponding to the areal capacity of 2.53 mA h cm^{-2} at 0.1C.[227] Remarkably, a superior capacity of 123 mA h g^{-1} (1.9 mA h cm^{-2}) at 2C was retained, suggesting its fast-charging capability and high-power application (Fig. 15i and j). It should be mentioned that the fiber LIMBs integrated into fabrics could normally drive a LED under bending condition, enabling the prolonged random twisting states. Therefore, the emerging 3D-printed fiber-based LIMBs open a new approach to construct high-performance and flexible power sources for next-generation smart microelectronics.

3D-printed Na-ion micro-battery

As an alternative to LIMB, NIMB is considered a next-generation miniaturized power source to satisfy the rapid and on-going development of microelectronics and microsystems due to its low cost, abundant sodium source, and similar working mechanism to LIMB.[12] To address the limited mass loading of active materials in thin microelectrodes and poor ion/electron conductivity in thick microelectrodes, our group demonstrated a prototype of fully 3D-printed interdigital NIMBs based on elaborate thick microelectrodes (~1200 μm) with an ultra-high areal mass loading of up to 60 mg cm^{-2}, showing 3D interconnected conductive networks to boost the areal capacity and rate capability (Fig. 16a).[33] Printable electrode inks and electrolyte inks with appropriate viscosity and rheological properties have been developed to print high-loading microelectrodes, customizable geometries (Fig. 16c and d), and high-ionic-conductivity ionogel electrolytes. The 1D CNTs and 2D graphene could form efficient electron/ion transport channels in the microelectrodes and enhance the reaction kinetics and promote the utilization rate of materials (Fig. 16b). As a consequence, the as-fabricated NIMBs showed a high areal capacity of 4.5 mA h cm^{-2} at 2 mA cm^{-2}, outstanding rate capability with an excellent areal capacity of 3.6 mA h cm^{-2} at a high current

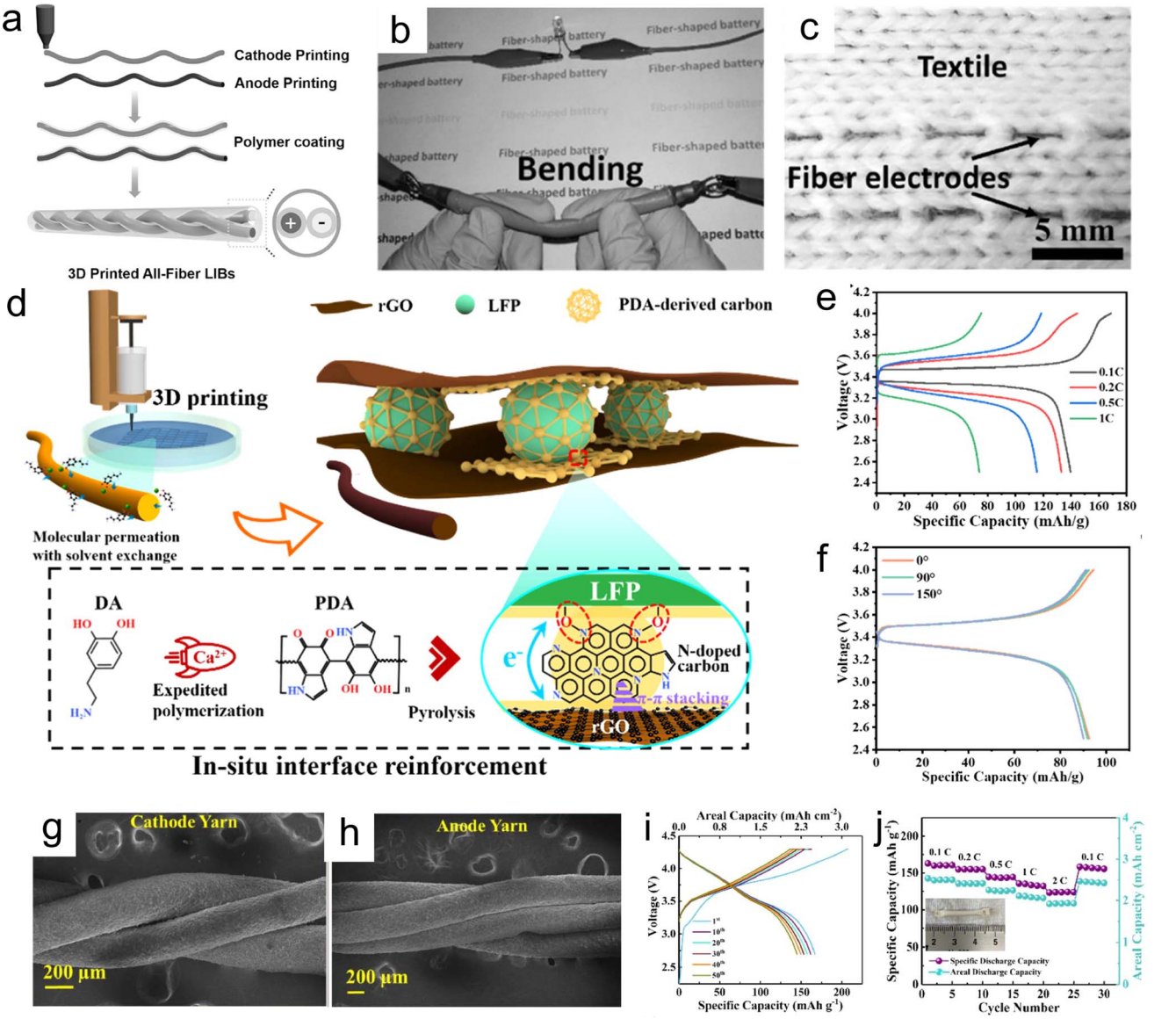

Fig. 15 3D-printed fiber-based LIMBs. (a) Schematic of the fabrication process of 3D-printed fiber-based LIMBs. Photographs of 3D-printed fiber-based LIMBs lighting up a LED in the bent state (b) and integrated into textile fabrics (c). Reproduced from ref. 133. Copyright 2017, Wiley-VCH. (d) Schematic of interface reinforcement for 3D-printed fiber electrodes. (e) GCD profiles of PDA@LFP cathodes at different current densities. (f) GCD profiles in various bending states. Reproduced from ref. 226. Copyright 2023, Elsevier. (g and h) SEM images of twisted electrode yarns. (i) GCD profiles of fabricated NCM811||graphite full cell at various cycling numbers. (j) Rate capability of fabricated NCM811||graphite full cell. Reproduced from ref. 227. Copyright 2021, Elsevier.

density of 40 mA cm^{-2} and exceptional cycling stability for 6000 cycles (Fig. 16e). Moreover, the 3D-printed NIMBs with 100-micron-level thick microelectrodes still exhibited excellent mechanical flexibility (Fig. 16f), which could be ascribed to the strong interface coupling between the electrode/electrolyte and electrode materials/conductive additives, and the porous networks buffering the stress. To further simplify the preparation procedure, Ding *et al.* reported a coaxial 3D printing method to fabricate all-in-one fiber NIMBs using SiO_2 separator ink and NVP electrode inks (Fig. 16g).[228] The 3D-printed symmetric NIMBs exhibited a high specific capacity of 50 mA h g^{-1} (based on the weight of the cathode, anode and electrolyte) at 100 mA g^{-1} and long cycling stability (Fig. 16h and i). This coaxial 3D printing strategy greatly improved the fabrication efficiency and economized the fabrication cost, becoming an attractive route to construct all-in-one fiber-based energy storage devices for multi-functional micro-systems.

3D-printed Zn-based micro-battery

In addition to the aforementioned alkali-ion MBs, multivalent-ion batteries have been also intensively developed recently, such as Zn^{2+}, Mg^{2+}, Ca^{2+} and Al^{3+}, which have high safety, low cost and abundant sources.[229,230] Nevertheless, 3D-printed multivalent-ion MBs only focused on Zn-based MBs, including Zn–Ag,[220] Zn-ion,[215] and Zn–air batteries.[221] Notably, the printed

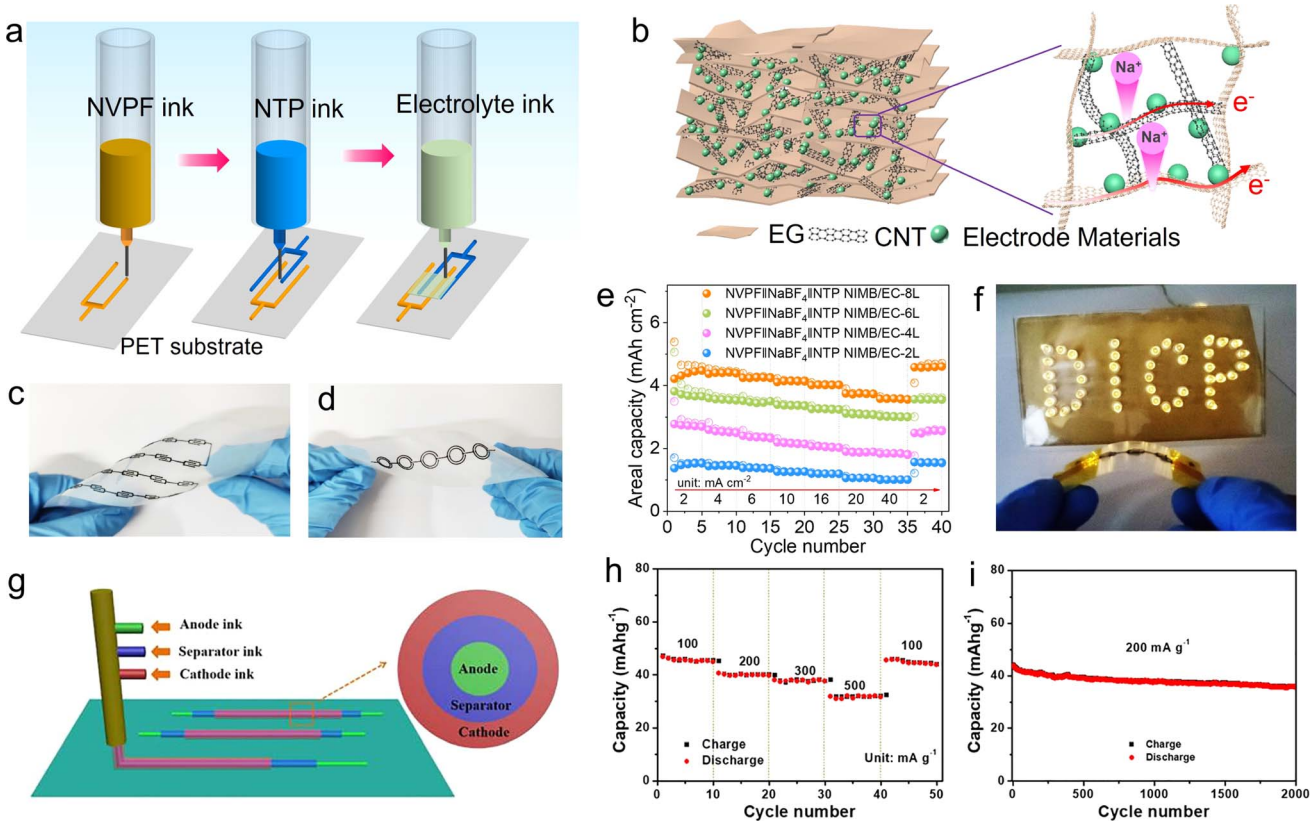

Fig. 16 3D-printed NIMBs. (a) Schematic of the fabrication process of 3D-printed interdigital NIMBs including cathodes, anodes and electrolytes. (b) Schematic illustration of the conductive networks in thick microelectrodes. (c and d) Photographs of customizable shapes of 3D-printed electrodes. (e) Rate capability of 3D-printed NIMBs with different electrode thickness. (f) Photograph of the letters "DICP" powered by three serial NIMBs. Reproduced from ref. 33. Copyright 2022, Wiley-VCH. (g) Schematic of the fabrication process of 3D-printed fiber NIMBs. Rate capability (h) and cycling performance tested at 200 mA g^{-1} (i) of fiber batteries. Reproduced from ref. 228. Copyright 2022, Elsevier.

Zn–Ag system is not only the first printed Zn-based MB, but also the first 3D-printed MB in 2009.[220] Ho *et al.* demonstrated a prototype of printed Zn–Ag MBs with high aspect ratio pillars by IJP method. The as-assembled array-structured Zn–Ag MBs showed an increased capacity compared to the planar configuration, delivering a high energy density of 300 W h kg^{-1}. This printed Zn–Ag MB pioneered printable MBs and stimulated the booming research on high-energy printable microscale power sources for wearable microelectronics. Subsequently, similar Zn–Ag MBs with a planar structure were printed *via* the DIW technique, delivering a high areal energy density of 4.1 mWh cm^{-2} at 1.8 mA cm^{-2}.[231] Recently, Guo *et al.* proposed a combined fabrication strategy involving 3D printing and electroless deposition to fabricate interdigital-type Zn–MnO_2 MBs using an Au/Ni current collector with low sheet resistance on a paper substrate (Fig. 17a).[232] The MnO_2 cathodes and Zn anodes were uniformly deposited on highly conductive current collectors, exhibiting a nanowire and nanosheet morphology, respectively. Due to the fast ion transfer in the nanostructured electrode materials, the printed Zn–MnO_2 MBs exhibited a high energy density of 168 μW h cm^{-2}, good cycling performance with a capacity retention of over 84% after 2000 cycles, and exceptional mechanical stability under extremely bending states. Interestingly, the multi-nozzle printer was capable of easily manufacturing different-structured Zn–MnO_2 MBs, such as single cell, tandem cell and parallel structure, realizing an adjustable voltage and capacity output for different application requirements.[235] It should be noted that the Zn dendrite issues formed on the planar substrate usually weaken the cycling stability of Zn-based MBs. For electrode optimization, Jin *et al.* designed an rGO-based framework with Cu modification for uniform Zn deposition by DIW printing.[233] In the symmetric cells of the Cu-modified Zn anodes, a long lifespan over 1200 h and high rate capability with 20 mA cm^{-2} were achieved (Fig. 17b and c), indicating fast and reversible Zn ion kinetics. These excellent results were ascribed to the increased zincophilic sites and large specific area of Cu-modified frameworks to buffer volume change and regulate the current distribution. Furthermore, calcium vanadate nanoribbon was used to prepare cathode inks to construct 3D-printed ZIMBs. With an increase the number of printed layers from 1 to 4 layers, the areal capacity of ZIMBs rose from 3.2 mA h cm^{-2} to 14.9 mA h cm^{-2} at 0.5 mA cm^{-2} (Fig. 17d). In addition, the 3D-printed ZIMBs delivered an excellent energy density of 6.04 mW h cm^{-2}, exceeding that of the reported MBs, which could power an LED integrated into a bracelet. Considering both material design and ink regulation, Zhao *et al.* developed an F/Ce co-doped V_2O_5 cathode with enhanced electrical conductivity

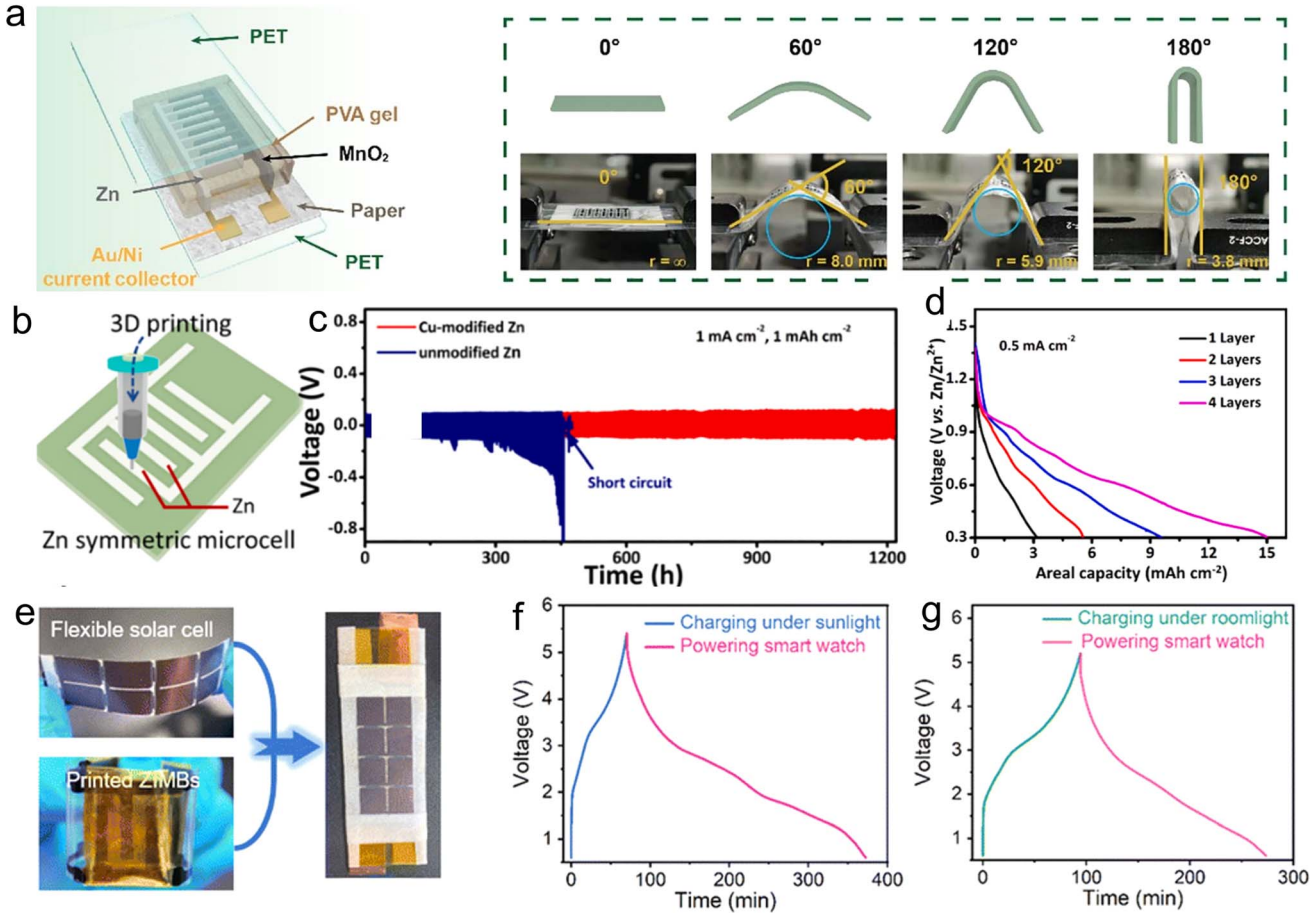

Fig. 17 3D-printed Zn-based MBs. (a) Schematic of the 3D-printed planar Zn–MnO_2 MBs (left) and photographs of Zn–MnO_2 MBs under different bending states (right). Reproduced from ref. 232. Copyright 2022, Elsevier. (b) Schematic of 3D-printed Zn symmetric cells. (c) Voltage profiles of 3D-printed Cu-modified Zn symmetric cells at 1 mA cm^{-2} and 1 mA h cm^{-2}. (d) Galvanostatic discharge profiles of 3D-printed ZIMBs with different layers. Reproduced from ref. 233. Copyright 2022, Elsevier. (e) Photographs of the 3D-printed ZIMBs integrated into a self-powered smart watch. Charging profiles under (f) sunlight and (g) room light of the ZIMBs powering the smart watch. Reproduced from ref. 234. Copyright 2023, The Royal Society of Chemistry.

and structural stability to mix carbon black and CNTs, forming highly conductive cathode inks.[234] The double-component conductive additives tightly wrapped the cathode nanoparticles, promoting fast charge transfer in the 3D-printed thick electrodes. As a result, the as-fabricated ZIMBs with $Zn(CF_3SO_3)_2$/PVA gel electrolyte delivered a satisfactory energy density of 8.1 mW h cm^{-2} and outstanding capacity retention of over 97% after 2000 cycles. To demonstrate the potential application of ZIMBs in microelectronics, a self-sustained micro-system was integrated with a flexible solar cell to power a smart watch (Fig. 17e). As shown in Fig. 17f and g, this elaborate micro-system could be charged to 5.2 V under both sunlight and room light, enabling it to support the operation of the smart watch. It was certified that the energy consumption of the devices was self-sufficient for steady operation all day. Furthermore, self-powered gas/temperature/pressure sensor-integrated systems could be manufactured using a printing method,[9,53,236] having a wide range of applications for human health monitoring.

Conclusions and perspective

As a class of innovative fabrication techniques, the 3D printing strategy can revolutionize design and structure at multi-scales, ranging from materials, electrodes and devices to systems, thus attracting widespread attention. In this review, we summarized the latest developments in 3D-printed MBs from the aspects of printing technology, printable components, printed MBs and their applications. The goal was facilitating a deep understanding 3D-printed MBs and their unique structures and applications in the relevant research community. The rapid progress in printable MBs has witnessed a series of technological progress, including optimizing the appropriate printing technology of 3D battery products, and realizing a printable battery module and the architecture and configuration at the full battery level. With the advancement of printing methods, there is a growing pursuit of a synthetic understanding of the design principles, involving printable materials, corresponding printing methods and printable units, and the

material-device-performance relationship.[237–239] Based on this, we propose the further development directions and prospects for architecting high-performance 3D-printed MBs.

In the case of printable materials and inks, currently research is mainly focused on the electrode materials of the cathode and anode materials of LIBs. To obtain higher-energy-density printable batteries, new active materials should be developed for novel battery systems, such as sulfur/selenium cathodes for Li–S/Se batteries.[99,240] In the manufacturing process of inks, different printing methods have varying requirements for the properties of active materials, *e.g.*, particle size and surface groups. The large-scale and low-cost production of high-quality materials with ideal performance have become the foundation to realize printable MBs. Besides, most reported 3D-printed electrodes exhibited poor mechanical strength, which impedes further device assembly. Therefore, future research should pay more attention to the construction of 3D-printed electrodes with both excellent mechanical properties and high electrochemical properties. Remarkably, the dispersion state and rheological properties of the battery component inks, as well as fluid dynamics and dry dynamics, have a significant effect on the quality/reliability of the printed electrodes and the electron/ion channels in the printed battery components. At present, realizing all-printed energy devices remains a challenge, in which most printing processes can only create one or two printable components, such as electrodes and electrolytes, and cannot manufacture the entire device *via* printing methods. It is necessary to ensure that all the units (electrodes, electrolytes/separators, current collectors, and packaging materials) in the energy storage device could be printed simultaneously.

In the case of novel printing technology, DIW technology is mostly used in patterning electrodes and electrolytes, exhibiting a low printing resolution at the 100-micron level. To architecture compact and fine microelectrodes, it is inevitable to develop high-resolution printing technology to make the accuracy level reach to 1 μm. In addition to the popular DIW printing, other printing technologies need to be further explored for device fabrication, such as electrohydrodynamic (EHD),[241] which are hopeful to construct a high-resolution geometry. In addition, the emerging 4D printing technology will permit the 3D-printed structure to change its configuration or function over the time in response to an external field, such as thermal, magnetic, light and electric fields.[242] Once the device structure is changed, it may further improve the performance of printed MBs. Furthermore, it is of great significance to construct a complete printing battery database based on the current printing technology, offering key directions and guidance to construct all-3D-printed customizable MBs. For instance, IJP and DIW processes have excellent multi-material printing capabilities, which can be used to prepare suitable electrode ink, electrolyte ink, and even current collector ink to create the key components of MBs. The development of an integrated, multi-functional printing chain composed of different printing techniques is a promising way to realize fully printed MBs.

In the case of the electrode structure or configuration, the current configuration of MBs mainly includes fiber, planar, and sandwich structures.[243] Different configurations of MBs can meet the requirements of distinct application scenarios, where the fiber type is more suitable for wearable fabric electronics, the planar type is well-matched for ultrathin and customized electronic devices, and the sandwich type is more appropriate for flexible electronic devices with high energy density. 3D-configuration MBs are more conducive to ion transfer, and can build a 3D electron/ion network structure, while considering the low interface resistance between the electrode and electrolyte, and the integrability with microelectronics device on the same substrate.[51] It will be very promising to synergistically combine the emerging 3D printing technology with traditional technologies. A thicker and porous electrode can obtain a higher areal energy density and power density, but abundant porous structures will affect the stacking density of the electrode and reduce the volumetric energy density of MBs. For example, by combining 3D printing technology with capsule shrinkage phenomenon, the pore structure can be accurately regulated in a thick electrode, obtaining both high areal and volumetric energy density, and high power density for MBs.[244] In addition, when the geometric structure expands to customizable shapes, the software design and simulation of the structure are also important to ensure their optimal performance. Developing appropriate models and simulation software will promote the true customization of electronic devices.

Considering mechanism study, it is capable of providing fundamental theoretical insight for improving the overall performance of the device by exploring new-type battery configurations, studying the reaction mechanism of the electrode and its reaction dynamics, and further analyzing the interface chemistry between the electrode and electrolyte. Planar microscale energy storage devices are ideal electrochemical models to conduct *in situ* research on the charge storage mechanism and the failure mechanism of the electrode material.[12,18,245] Their coplane electrode characteristic eliminates the separators in the vertical direction, realizing the simultaneous observation of the cathode and anode evolution, ion transfer, and interface transportation information. Therefore, developing planar microscale devices used for *in situ* detection provides a new research platform to clarify the microscopic mechanism and the electrochemical reaction process.

Regarding new integrated microsystems, they can provide new prospects for the development of high-performance integrated electronic systems by the combination of printed power supply with human health sensors, wireless charging and artificial intelligence units. To this end, research should be committed to further improving the diversity, mechanical flexibility, biocompatibility and toxicology design. In addition, the integration of various functional devices into a whole electronic system usually requires complex circuit design, which may lead to unnecessary energy loss and volume increase. Building a printed form factor-free power supply is an effective way to solve this problem because it can eliminate or minimize power management circuits and external interconnect circuits. Nevertheless, further investigation is highly required to achieve electrical compatibility with various electronic equipment in a limited area and spacing.

Author contributions

Jiaxin Ma: writing – original draft preparation, visualization, review & editing. Shuanghao Zheng: writing – original draft preparation, supervision, review & editing. Yinghua Fu, Xiao Wang & Jieqiong Qin: visualization, review & editing. Zhong-Shuai Wu: writing – original draft preparation, supervision, review & editing, funding acquisition.

Conflicts of interest

There are no conflicts to declare.

Acknowledgements

This work was financially supported by the National Natural Science Foundation of China (Grants 22075279, 22279137, 22125903, 22209173, 22109040), National Key R&D Program of China (Grants 2022YFA1504100, 2023YFB4005204), Dalian Innovation Support Plan for High Level Talents (2019RT09), Dalian National Laboratory For Clean Energy (DNL), CAS, DNL Cooperation Fund, CAS (DNL202016, DNL202019), and DICP (DICP I2020032).

References

1 G. J. Snyder, J. R. Lim, C. K. Huang and J. P. Fleurial, *Nat. Mater.*, 2003, **2**, 528–531.
2 V. K. Bandari, Y. Nan, D. Karnaushenko, Y. Hong, B. Sun, F. Striggow, D. D. Karnaushenko, C. Becker, M. Faghih, M. Medina-Sánchez, F. Zhu and O. G. Schmidt, *Nat. Electron.*, 2020, **3**, 172–180.
3 B. Dieny, I. L. Prejbeanu, K. Garello, P. Gambardella, P. Freitas, R. Lehndorff, W. Raberg, U. Ebels, S. O. Demokritov, J. Akerman, A. Deac, P. Pirro, C. Adelmann, A. Anane, A. V. Chumak, A. Hirohata, S. Mangin, S. O. Valenzuela, M. C. Onbaşlı, M. d'Aquino, G. Prenat, G. Finocchio, L. Lopez-Diaz, R. Chantrell, O. Chubykalo-Fesenko and P. Bortolotti, *Nat. Electron.*, 2020, **3**, 446–459.
4 M. Beidaghi and Y. Gogotsi, *Energy Environ. Sci.*, 2014, **7**, 867.
5 Z. S. Wu, K. Parvez, X. Feng and K. Mullen, *Nat. Commun.*, 2013, **4**, 2487.
6 W. Gao, N. Singh, L. Song, Z. Liu, A. L. Reddy, L. Ci, R. Vajtai, Q. Zhang, B. Wei and P. M. Ajayan, *Nat. Nanotechnol.*, 2011, **6**, 496–500.
7 J. Ren, L. Li, C. Chen, X. Chen, Z. Cai, L. Qiu, Y. Wang, X. Zhu and H. Peng, *Adv. Mater.*, 2013, **25**, 1155–1159.
8 S. Lee, H. W. Choi, C. L. Figueiredo, D.-W. Shin, F. M. Moncunill, K. Ullrich, S. Sinopoli, P. Jovančić, J. Yang, H. Lee, M. Eisenreich, U. Emanuele, S. Nicotera, A. Santos, R. Igreja, A. Marrani, R. Momentè, J. Gomes, S.-M. Jung, S. D. Han, S. Y. Bang, S. Zhan, W. Harden-Chaters, Y.-H. Suh, X.-B. Fan, T. H. Lee, J.-W. Jo, Y. Kim, A. Costantino, V. G. Candel, N. Durães, S. Meyer, C.-H. Kim, M. Lucassen, A. Nejim, D. Jiménez, M. Springer, Y.-W. Lee, G.-H. An, Y. Choi, J. I. Sohn, S. Cha, M. Chhowalla, G. A. J. Amaratunga, L. G. Occhipinti, P. Barquinha, E. Fortunato, R. Martins and J. M. Kim, *Sci. Adv.*, 2023, **9**, eadf4049.
9 X. Shi, P. Das and Z.-S. Wu, *ACS Energy Lett.*, 2022, **7**, 267–281.
10 M. F. El-Kady, M. Ihns, M. Li, J. Y. Hwang, M. F. Mousavi, L. Chaney, A. T. Lech and R. B. Kaner, *Proc. Natl. Acad. Sci. U. S. A.*, 2015, **112**, 4233–4238.
11 X. Cai, Y. Liu, J. Zha, F. Tan, B. Zhang, W. Yan, J. Zhao, B. Lu, J. Zhou and C. Tan, *Adv. Funct. Mater.*, 2023, **33**, 2303009.
12 S. Zheng, H. Huang, Y. Dong, S. Wang, F. Zhou, J. Qin, C. Sun, Y. Yu, Z.-S. Wu and X. Bao, *Energy Environ. Sci.*, 2020, **13**, 821–829.
13 Z. Tian, Z. Sun, Y. Shao, L. Gao, R. Huang, Y. Shao, R. B. Kaner and J. Sun, *Energy Environ. Sci.*, 2021, **14**, 1602–1611.
14 K. Gerasopoulos, E. Pomerantseva, M. McCarthy, A. Brown, C. Wang, J. Culver and R. Ghodssi, *ACS Nano*, 2012, **6**, 6422–6432.
15 S. Zheng, X. Shi, P. Das, Z. S. Wu and X. Bao, *Adv. Mater.*, 2019, **31**, e1900583.
16 J. Ma, S. Zheng, P. Das, P. Lu, Y. Yu and Z.-S. Wu, *Small Struct.*, 2020, **1**, 2000053.
17 J. F. M. Oudenhoven, L. Baggetto and P. H. L. Notten, *Adv. Energy Mater.*, 2010, **1**, 10–33.
18 S. Zheng, Z.-S. Wu, F. Zhou, X. Wang, J. Ma, C. Liu, Y.-B. He and X. Bao, *Nano Energy*, 2018, **51**, 613–620.
19 X. Wang, S. Zheng, F. Zhou, J. Qin, X. Shi, S. Wang, C. Sun, X. Bao and Z.-S. Wu, *Natl. Sci. Rev.*, 2020, **7**, 64–72.
20 M. Zhu, J. Hu, Q. Lu, H. Dong, D. D. Karnaushenko, C. Becker, D. Karnaushenko, Y. Li, H. Tang, Z. Qu, J. Ge and O. G. Schmidt, *Adv. Mater.*, 2021, **33**, e2007497.
21 M. Yao, Z. Yuan, S. Li, T. He, R. Wang, M. Yuan and Z. Niu, *Adv. Mater.*, 2021, **33**, 2008140.
22 S.-Y. Lee, K.-H. Choi, W.-S. Choi, Y. H. Kwon, H.-R. Jung, H.-C. Shin and J. Y. Kim, *Energy Environ. Sci.*, 2013, **6**, 2414.
23 H. Ning, J. H. Pikul, R. Zhang, X. Li, S. Xu, J. Wang, J. A. Rogers, W. P. King and P. V. Braun, *Proc. Natl. Acad. Sci. U. S. A.*, 2015, **112**, 6573–6578.
24 P. Sun, X. Li, J. Shao and P. V. Braun, *Adv. Mater.*, 2021, **33**, e2006229.
25 K. Brousse, P. L. Taberna and P. Simon, *J. Electrochem. Soc.*, 2022, **169**, 070534.
26 L. Zhao, Z. Liu, D. Chen, F. Liu, Z. Yang, X. Li, H. Yu, H. Liu and W. Zhou, *Nano-Micro Lett.*, 2021, **13**, 49.
27 X. Chen, Z. Hou, G. Li, W. Yu, Y. Xue, G. Niu, M. Xin, L. Yang, C. Meng and S. Guo, *Nano Energy*, 2022, **101**, 107606.
28 J. H. Pikul, H. Gang Zhang, J. Cho, P. V. Braun and W. P. King, *Nat. Commun.*, 2013, **4**, 1732.
29 R. Li, L. Li, R. Jia, K. Jiang, G. Shen and D. Chen, *Small Methods*, 2020, **4**, 2000363.
30 Y. Zhang, S. Zheng, F. Zhou, X. Shi, C. Dong, P. Das, J. Ma, K. Wang and Z. S. Wu, *Small*, 2022, **18**, e2104506.

31 S. Zheng, H. Wang, P. Das, Y. Zhang, Y. Cao, J. Ma, S. F. Liu and Z. S. Wu, *Adv. Mater.*, 2021, **33**, e2005449.
32 K. Sun, T. S. Wei, B. Y. Ahn, J. Y. Seo, S. J. Dillon and J. A. Lewis, *Adv. Mater.*, 2013, **25**, 4539–4543.
33 J. Ma, S. Zheng, L. Chi, Y. Liu, Y. Zhang, K. Wang and Z. S. Wu, *Adv. Mater.*, 2022, **34**, e2205569.
34 Y. Jiang, F. Guo, Y. Liu, Z. Xu and C. Gao, *SusMat*, 2021, **1**, 304–323.
35 Y. Yuan, L. Jiang, X. Li, P. Zuo, C. Xu, M. Tian, X. Zhang, S. Wang, B. Lu, C. Shao, B. Zhao, J. Zhang, L. Qu and T. Cui, *Nat. Commun.*, 2020, **11**, 6185.
36 W. Zhang, Y. Lei, F. Ming, Q. Jiang, P. M. F. J. Costa and H. N. Alshareef, *Adv. Energy Mater.*, 2018, **8**, 1801840.
37 S. Abdolhosseinzadeh, R. Schneider, A. Verma, J. Heier, F. Nuesch and C. J. Zhang, *Adv. Mater.*, 2020, **32**, e2000716.
38 J. Wang, F. Li, F. Zhu and O. G. Schmidt, *Small Methods*, 2019, **3**, 1800367.
39 C. Zhang, Y. Li, W. Kang, X. Liu and Q. Wang, *SusMat*, 2021, **1**, 127–147.
40 E. MacDonald and R. Wicker, *Science*, 2016, **353**, aaf2093.
41 M. Zastrow, *Nature*, 2020, **578**, 20–23.
42 J. H. Martin, B. D. Yahata, J. M. Hundley, J. A. Mayer, T. A. Schaedler and T. M. Pollock, *Nature*, 2017, **549**, 365–369.
43 M. A. Skylar-Scott, J. Mueller, C. W. Visser and J. A. Lewis, *Nature*, 2019, **575**, 330–335.
44 W. Zhang, H. Liu, X. Zhang, X. Li, G. Zhang and P. Cao, *Adv. Funct. Mater.*, 2021, **31**, 2104909.
45 X. Xu, Y. H. Tan, J. Ding and C. Guan, *Energy Environ. Mater.*, 2021, **5**, 427–438.
46 E. Fantino, A. Chiappone, I. Roppolo, D. Manfredi, R. Bongiovanni, C. F. Pirri and F. Calignano, *Adv. Mater.*, 2016, **28**, 3712–3717.
47 Y. Liu, S. Zheng, J. Ma, X. Wang, L. Zhang, P. Das, K. Wang and Z. S. Wu, *Adv. Energy Mater.*, 2022, **12**, 2200341.
48 M. Zhang, T. Xu, D. Wang, T. Yao, Z. Xu, Q. Liu, L. Shen and Y. Yu, *Adv. Mater.*, 2023, **35**, 2209963.
49 Y. Liu, S. Zheng, J. Ma, Y. Zhu, J. Wang, X. Feng and Z.-S. Wu, *J. Energy Chem.*, 2021, **63**, 514–520.
50 T. Chu, S. Park and K. Fu, *Carbon Energy*, 2021, **3**, 424–439.
51 H. Sun, J. Zhu, D. Baumann, L. Peng, Y. Xu, I. Shakir, Y. Huang and X. Duan, *Nat. Rev. Mater.*, 2019, **4**, 45–60.
52 M. S. Saleh, J. Li, J. Park and R. Panat, *Addit. Manuf.*, 2018, **23**, 70–78.
53 J. Ma, S. Zheng, Y. Cao, Y. Zhu, P. Das, H. Wang, Y. Liu, J. Wang, L. Chi, S. Liu and Z. S. Wu, *Adv. Energy Mater.*, 2021, **11**, 2100746.
54 Z. Tian, X. Tong, G. Sheng, Y. Shao, L. Yu, V. Tung, J. Sun, R. B. Kaner and Z. Liu, *Nat. Commun.*, 2019, **10**, 4913.
55 G. Hu, J. Kang, L. W. T. Ng, X. Zhu, R. C. T. Howe, C. G. Jones, M. C. Hersam and T. Hasan, *Chem. Soc. Rev.*, 2018, **47**, 3265–3300.
56 K.-H. Choi, D. B. Ahn and S.-Y. Lee, *ACS Energy Lett.*, 2017, **3**, 220–236.
57 G. Zhang, X. Zhang, H. Liu, J. Li, Y. Chen and H. Duan, *Adv. Energy Mater.*, 2021, **11**, 2003927.
58 J. Ma, S. Zheng, F. Zhou, Y. Zhu, P. Das, R. Huang, L. Zhang, X. Wang, H. Wang, Y. Cui and Z.-S. Wu, *Energy Storage Mater.*, 2022, **54**, 304–312.
59 Z. Lyu, G. J. H. Lim, J. J. Koh, Y. Li, Y. Ma, J. Ding, J. Wang, Z. Hu, J. Wang, W. Chen and Y. Chen, *Joule*, 2021, **5**, 89–114.
60 X. Gao, M. Zheng, X. Yang, R. Sun, J. Zhang and X. Sun, *Mater. Today*, 2022, **59**, 161–181.
61 Y. Lin, Y. Gao and Z. Fan, *Adv. Mater.*, 2017, **29**, 1701736.
62 Y. Zhu, J. Qin, G. Shi, C. Sun, M. Ingram, S. Qian, J. Lu and S. Z. Y. L. Zhong 2, *Carbon Energy*, 2022, **4**, 1242–1261.
63 X. Tian, J. Jin, S. Yuan, C. K. Chua, S. B. Tor and K. Zhou, *Adv. Energy Mater.*, 2017, **7**, 1700127.
64 M. Singh, H. M. Haverinen, P. Dhagat and G. E. Jabbour, *Adv. Mater.*, 2010, **22**, 673–685.
65 L. J. Deiner and T. L. Reitz, *Adv. Eng. Mater.*, 2017, **19**, 1600878.
66 M. Saadi, A. Maguire, N. T. Pottackal, M. S. H. Thakur, M. M. Ikram, A. J. Hart, P. M. Ajayan and M. M. Rahman, *Adv. Mater.*, 2022, **34**, e2108855.
67 V. Dhinakaran, K. P. Manoj Kumar, P. M. Bupathi Ram, M. Ravichandran and M. Vinayagamoorthy, *Mater. Today: Proc.*, 2020, **27**, 752–756.
68 S. Das, *Adv. Eng. Mater.*, 2003, **5**, 701–711.
69 M. W. Khaing, J. Y. H. Fuh and L. Lu, *J. Mater. Process. Technol.*, 2001, **113**, 269–272.
70 T. Chartier, C. Chaput, F. Doreau and M. Loiseau, *J. Mater. Sci.*, 2002, **37**, 3141–3147.
71 Q. Mu, L. Wang, C. K. Dunn, X. Kuang, F. Duan, Z. Zhang, H. J. Qi and T. Wang, *Addit. Manuf.*, 2017, **18**, 74–83.
72 G. Williams, M. Hunt, B. Boehm, A. May, M. Taverne, D. Ho, S. Giblin, D. Read, J. Rarity, R. Allenspach and S. Ladak, *Nano Res.*, 2017, **11**, 845–854.
73 B. Dermeik and N. Travitzky, *Adv. Eng. Mater.*, 2020, **22**, 2000256.
74 A. Mostafaei, A. M. Elliott, J. E. Barnes, F. Li, W. Tan, C. L. Cramer, P. Nandwana and M. Chmielus, *Prog. Mater. Sci.*, 2021, **119**, 100707.
75 D. Svetlizky, M. Das, B. Zheng, A. L. Vyatskikh, S. Bose, A. Bandyopadhyay, J. M. Schoenung, E. J. Lavernia and N. Eliaz, *Mater. Today*, 2021, **49**, 271–295.
76 D. S. Kolchanov, I. Mitrofanov, A. Kim, Y. Koshtyal, A. Rumyantsev, E. Sergeeva, A. Vinogradov, A. Popovich and M. Y. Maximov, *Energy Technol.*, 2019, **8**, 1901086.
77 J. Yan, S. Huang, Y. V. Lim, T. Xu, D. Kong, X. Li, H. Y. Yang and Y. Wang, *Mater. Today*, 2022, **54**, 110–152.
78 A. Maurel, S. Grugeon, B. Fleutot, M. Courty, K. Prashantha, H. Tortajada, M. Armand, S. Panier and L. Dupont, *Sci. Rep.*, 2019, **9**, 18031.
79 K. A. Acord, A. D. Dupuy, U. Scipioni Bertoli, B. Zheng, W. C. West, Q. N. Chen, A. A. Shapiro and J. M. Schoenung, *J. Mater. Process. Technol.*, 2021, **288**, 116827.
80 Y. Pang, Y. Cao, Y. Chu, M. Liu, K. Snyder, D. MacKenzie and C. Cao, *Adv. Funct. Mater.*, 2019, **30**, 1906244.
81 J. A. Lewis, *Adv. Funct. Mater.*, 2006, **16**, 2193–2204.
82 A. M'Barki, L. Bocquet and A. Stevenson, *Sci. Rep.*, 2017, **7**, 6017.

83 M. Tang, Z. Zhong and C. Ke, *Chem. Soc. Rev.*, 2023, **52**, 1614–1649.
84 Z. Liu, X. Tian, M. Liu, S. Duan, Y. Ren, H. Ma, K. Tang, J. Shi, S. Hou, H. Jin and G. Cao, *Small*, 2021, **17**, e2002866.
85 A. Mantelli, A. Romani, R. Suriano, M. Levi and S. Turri, *Adv. Eng. Mater.*, 2021, **23**, 2100116.
86 D. Cao, Y. Xing, K. Tantratian, X. Wang, Y. Ma, A. Mukhopadhyay, Z. Cheng, Q. Zhang, Y. Jiao, L. Chen and H. Zhu, *Adv. Mater.*, 2019, **31**, e1807313.
87 M. Cheng, A. Ramasubramanian, M. G. Rasul, Y. Jiang, Y. Yuan, T. Foroozan, R. Deivanayagam, M. Tamadoni Saray, R. Rojaee, B. Song, V. R. Yurkiv, Y. Pan, F. Mashayek and R. Shahbazian-Yassar, *Adv. Funct. Mater.*, 2020, **31**, 2006683.
88 H. Li and J. Liang, *Adv. Mater.*, 2019, **32**, e1805864.
89 R. Steller and J. Iwko, *Polym. Eng. Sci.*, 2018, **58**, 1446–1455.
90 F. Galindo-Rosales, *Appl. Sci.*, 2016, **6**, 206.
91 S. Abdolhosseinzadeh, X. Jiang, H. Zhang, J. Qiu and C. Zhang, *Mater. Today*, 2021, **48**, 214–240.
92 R. Steller and J. Iwko, *Polym. Eng. Sci.*, 2017, **58**, 1446–1455.
93 L. W. T. Ng, X. Zhu, G. Hu, N. Macadam, D. Um, T. C. Wu, F. Le Moal, C. Jones and T. Hasan, *Adv. Funct. Mater.*, 2019, **29**, 1807933.
94 M. L. Gardel, J. H. Shin, F. C. MacKintosh, L. Mahadevan, P. Matsudaira and D. A. Weitz, *Science*, 2004, **304**, 1301–1305.
95 Y. Lin, N. Phan-Thien, J. B. Lee and B. C. Khoo, *Langmuir*, 2015, **31**, 4791–4797.
96 H. Yuk and X. Zhao, *Adv. Mater.*, 2018, **30**, 1704028.
97 G. M. Gratson, F. García-Santamaría, V. Lousse, M. Xu, S. Fan, J. A. Lewis and P. V. Braun, *Adv. Mater.*, 2006, **18**, 461–465.
98 W. Yang, Y. Duan, J. Gao and Z. Yin, *Addit. Manuf.*, 2023, **77**, 103815.
99 C. Chen, J. Jiang, W. He, W. Lei, Q. Hao and X. Zhang, *Adv. Funct. Mater.*, 2020, **30**, 1909469.
100 R. B. Kristiawan, F. Imaduddin, D. Ariawan, Ubaidillah and Z. Arifin, *Open Eng.*, 2021, **11**, 639–649.
101 O. A. Mohamed, S. H. Masood and J. L. Bhowmik, *Adv. Manuf.*, 2015, **3**, 42–53.
102 T. Webbe Kerekes, H. Lim, W. Y. Joe and G. J. Yun, *Addit. Manuf.*, 2019, **25**, 532–544.
103 P. Calvert, *Chem. Mater.*, 2001, **13**, 3299–3305.
104 B. J. de Gans, P. C. Duineveld and U. S. Schubert, *Adv. Mater.*, 2004, **16**, 203–213.
105 Z. Yin, Y. Huang, N. Bu, X. Wang and Y. Xiong, *Chin. Sci. Bull.*, 2010, **55**, 3383–3407.
106 J. Dai, O. Ogbeide, N. Macadam, Q. Sun, W. Yu, Y. Li, B. L. Su, T. Hasan, X. Huang and W. Huang, *Chem. Soc. Rev.*, 2020, **49**, 1756–1789.
107 S. Kholghi Eshkalak, A. Chinnappan, W. A. D. M. Jayathilaka, M. Khatibzadeh, E. Kowsari and S. Ramakrishna, *Appl. Mater. Today*, 2017, **9**, 372–386.
108 X. Wang, M. Zhang, L. Zhang, J. Xu, X. Xiao and X. Zhang, *Mater. Today Commun.*, 2022, **31**, 103263.
109 S. Lee, T. Boeltken, A. K. Mogalicherla, U. Gerhards, P. Pfeifer and R. Dittmeyer, *Appl. Catal., A*, 2013, **467**, 69–75.
110 Y. Son, C. Kim, D. H. Yang and D. J. Ahn, *Langmuir*, 2008, **24**, 2900–2907.
111 C. J. Zhang, L. McKeon, M. P. Kremer, S. H. Park, O. Ronan, A. Seral-Ascaso, S. Barwich, C. O. Coileain, N. McEvoy, H. C. Nerl, B. Anasori, J. N. Coleman, Y. Gogotsi and V. Nicolosi, *Nat. Commun.*, 2019, **10**, 1795.
112 T. Vidmar, M. Topič, P. Dzik and U. Opara Krašovec, *Sol. Energy Mater. Sol. Cells*, 2014, **125**, 87–95.
113 P. J. Yunker, T. Still, M. A. Lohr and A. G. Yodh, *Nature*, 2011, **476**, 308–311.
114 N. Bhattacharjee, C. Parra-Cabrera, Y. T. Kim, A. P. Kuo and A. Folch, *Adv. Mater.*, 2018, **30**, 1800001.
115 H. Quan, T. Zhang, H. Xu, S. Luo, J. Nie and X. Zhu, *Bioact. Mater.*, 2020, **5**, 110–115.
116 Y. Sano, R. Matsuzaki, M. Ueda, A. Todoroki and Y. Hirano, *Addit. Manuf.*, 2018, **24**, 521–527.
117 A. Bagheri and J. Jin, *ACS Appl. Polym. Mater.*, 2019, **1**, 593–611.
118 A. C. Uzcategui, A. Muralidharan, V. L. Ferguson, S. J. Bryant and R. R. McLeod, *Adv. Eng. Mater.*, 2018, **20**, 1800876.
119 B. B. Noble, A. C. Mater, L. M. Smith and M. L. Coote, *Polym. Chem.*, 2016, **7**, 6400–6412.
120 X. Zhang, Y. Xu, L. Li, B. Yan, J. Bao and A. Zhang, *J. Appl. Polym. Sci.*, 2019, **136**, 47487.
121 M. Peerzada, S. Abbasi, K. T. Lau and N. Hameed, *Ind. Eng. Chem. Res.*, 2020, **59**, 6375–6390.
122 D. Chen, Z. Lou, K. Jiang and G. Shen, *Adv. Funct. Mater.*, 2018, **28**, 1805596.
123 F. Wu, J. Maier and Y. Yu, *Chem. Soc. Rev.*, 2020, **49**, 1569–1614.
124 X. Li, S. Ling, L. Zeng, H. He, X. Liu and C. Zhang, *Adv. Energy Mater.*, 2022, **12**, 2200233.
125 J. Ding, K. Shen, Z. Du, B. Li and S. Yang, *ACS Appl. Mater. Interfaces*, 2017, **9**, 41871–41877.
126 H. Yang, Y. Wan, K. Sun, M. Zhang, C. Wang, Z. He, Q. Li, N. Wang, Y. Zhang, H. Hu and M. Wu, *Adv. Funct. Mater.*, 2023, **33**, 2215076.
127 J. Cai, J. Jin, Z. Fan, C. Li, Z. Shi, J. Sun and Z. Liu, *Adv. Mater.*, 2020, **32**, e2005967.
128 S. D. Lacey, D. J. Kirsch, Y. Li, J. T. Morgenstern, B. C. Zarket, Y. Yao, J. Dai, L. Q. Garcia, B. Liu, T. Gao, S. Xu, S. R. Raghavan, J. W. Connell, Y. Lin and L. Hu, *Adv. Mater.*, 2018, **30**, e1705651.
129 P. E. Delannoy, B. Riou, T. Brousse, J. Le Bideau, D. Guyomard and B. Lestriez, *J. Power Sources*, 2015, **287**, 261–268.
130 K. Fu, Y. Wang, C. Yan, Y. Yao, Y. Chen, J. Dai, S. Lacey, Y. Wang, J. Wan, T. Li, Z. Wang, Y. Xu and L. Hu, *Adv. Mater.*, 2016, **28**, 2587–2594.
131 J. Wang, Q. Sun, X. Gao, C. Wang, W. Li, F. B. Holness, M. Zheng, R. Li, A. D. Price, X. Sun, T.-K. Sham and X. Sun, *ACS Appl. Mater. Interfaces*, 2018, **10**, 39794–39801.
132 R. R. Kohlmeyer, A. J. Blake, J. O. Hardin, E. A. Carmona, J. Carpena-Núñez, B. Maruyama, J. Daniel Berrigan, H. Huang and M. F. Durstock, *J. Mater. Chem. A*, 2016, **4**, 16856–16864.

133 Y. Wang, C. Chen, H. Xie, T. Gao, Y. Yao, G. Pastel, X. Han, Y. Li, J. Zhao, K. Fu and L. Hu, *Adv. Funct. Mater.*, 2017, **27**, 1703140.
134 J. Huang, J. Yang, W. Li, W. Cai and Z. Jiang, *Thin Solid Films*, 2008, **516**, 3314–3319.
135 D. W. Yee, M. A. Citrin, Z. W. Taylor, M. A. Saccone, V. L. Tovmasyan and J. R. Greer, *Adv. Mater. Technol.*, 2021, **6**, 2000791.
136 J. Li, M. C. Leu, R. Panat and J. Park, *Mater. Des.*, 2017, **119**, 417–424.
137 J. Hu, Y. Jiang, S. Cui, Y. Duan, T. Liu, H. Guo, L. Lin, Y. Lin, J. Zheng, K. Amine and F. Pan, *Adv. Energy Mater.*, 2016, **6**, 1600856.
138 S. Praveen, P. Santhoshkumar, Y. C. Joe, C. Senthil and C. W. Lee, *Appl. Mater. Today*, 2020, **20**, 100688.
139 S. Praveen, G. S. Sim, N. Shaji, M. Nanthagopal and C. W. Lee, *Appl. Mater. Today*, 2022, **26**, 100980.
140 X. Tian, T. Wang, H. Ma, K. Tang, S. Hou, H. Jin and G. Cao, *J. Mater. Chem. A*, 2021, **9**, 16086–16092.
141 S. Ao, Z. Guo, Y. Song, D. Fang and Y. Bao, *ACS Appl. Energy Mater.*, 2022, **5**, 6970–6979.
142 S. Ling, X. Li, T. Zhou, R. Yuan, S. Sun, H. He and C. Zhang, *Adv. Mater.*, 2023, **35**, e2211201.
143 H. Ragones, S. Menkin, Y. Kamir, A. Gladkikh, T. Mukra, G. Kosa and D. Golodnitsky, *Sustainable Energy Fuels*, 2018, **2**, 1542–1549.
144 V. Gupta, F. Alam, P. Verma, A. M. Kannan and S. Kumar, *J. Power Sources*, 2021, **494**, 229625.
145 J. F. Valera-Jiménez, J. C. Pérez-Flores, M. Castro-García and J. Canales-Vázquez, *Appl. Mater. Today*, 2021, **25**, 101243.
146 X. Hu, Y. Chen, W. Xu, Y. Zhu, D. Kim, Y. Fan, B. Yu and Y. Chen, *Small*, 2023, **19**, e2301604.
147 I. Ben-Barak, Y. Kamir, S. Menkin, M. Goor, I. Shekhtman, T. Ripenbein, E. Galun, D. Golodnitsky and E. Peled, *J. Electrochem. Soc.*, 2018, **166**, A5059–A5064.
148 F. Su, F. Xing, X. Wang, F. Liu, L. Zhang and Z.-S. Wu, *Energy Environ. Sci.*, 2023, **16**, 222–230.
149 M. P. Down, E. Martínez-Periñán, C. W. Foster, E. Lorenzo, G. C. Smith and C. E. Banks, *Adv. Energy Mater.*, 2019, **9**, 1803019.
150 H. Ma, X. Tian, T. Wang, K. Tang, Z. Liu, S. Hou, H. Jin and G. Cao, *Small*, 2021, **17**, e2100746.
151 W. Gao, J. Michalicka and M. Pumera, *Small*, 2022, **18**, e2105572.
152 C. A. Milroy, S. Jang, T. Fujimori, A. Dodabalapur and A. Manthiram, *Small*, 2017, **13**, 1603786.
153 X. Gao, Q. Sun, X. Yang, J. Liang, A. Koo, W. Li, J. Liang, J. Wang, R. Li and F. B. Holness, *Nano energy*, 2019, **56**, 595–603.
154 S. H. Kim, J. H. Kim, S. J. Cho and S. Y. Lee, *Adv. Energy Mater.*, 2019, **9**, 1901841.
155 Y. Ouyang, W. Zong, X. Zhu, L. Mo, G. Chao, W. Fan, F. Lai, Y. E. Miao, T. Liu and Y. Yu, *Adv. Sci.*, 2022, **9**, e2203181.
156 W. Xi, J. Zhang, Y. Zhang, R. Wang, Y. Gong, B. He, H. Wang and J. Jin, *J. Mater. Chem. A*, 2023, **11**, 7679–7689.
157 X. Gao, X. Yang, S. Wang, Q. Sun, C. Zhao, X. Li, J. Liang, M. Zheng, Y. Zhao, J. Wang, M. Li, R. Li, T.-K. Sham and X. Sun, *J. Mater. Chem. A*, 2020, **8**, 278–286.
158 Z. Lyu, G. J. H. Lim, R. Guo, Z. Kou, T. Wang, C. Guan, J. Ding, W. Chen and J. Wang, *Adv. Funct. Mater.*, 2018, **29**, 1806658.
159 X. Lin, J. Wang, X. Gao, S. Wang, Q. Sun, J. Luo, C. Zhao, Y. Zhao, X. Yang, C. Wang, R. Li and X. Sun, *Chem. Mater.*, 2020, **32**, 3018–3027.
160 J. Zhang, X. L. Li, S. Fan, S. Huang, D. Yan, L. Liu, P. Valdivia y Alvarado and H. Y. Yang, *Mater. Today Energy*, 2020, **16**, 100407.
161 K. Shen, H. Mei, B. Li, J. Ding and S. Yang, *Adv. Energy Mater.*, 2018, **8**, 1701527.
162 L. Xue, L. Zeng, W. Kang, H. Chen, Y. Hu, Y. Li, W. Chen, T. Lei, Y. Yan, C. Yang, A. Hu, X. Wang, J. Xiong and C. Zhang, *Adv. Energy Mater.*, 2021, **11**, 2100420.
163 X. Gao, X. Yang, Q. Sun, J. Luo, J. Liang, W. Li, J. Wang, S. Wang, M. Li, R. Li, T.-K. Sham and X. Sun, *Energy Storage Mater.*, 2020, **24**, 682–688.
164 C. Liu, Y. Qiu, Y. Liu, K. Xu, N. Zhao, C. Lao, J. Shen and Z. Chen, *J. Adv. Ceram.*, 2022, **11**, 295–307.
165 C. Liu, F. Xu, Y. Liu, J. Ma, P. Liu, D. Wang, C. Lao and Z. Chen, *Electrochim. Acta*, 2019, **314**, 81–88.
166 C. Sun, S. Liu, X. Shi, C. Lai, J. Liang and Y. Chen, *Chem. Eng. J.*, 2020, **381**, 122641.
167 J. P. Mwizerwa, K. Xu, C. Liu, N. Zhao, Y. Li, P. Ndagijimana, Z. Chen and J. Shen, *Mater. Today Chem.*, 2023, **29**, 101483.
168 C. Liu, N. Zhao, K. Xu, Y. Li, J. P. Mwizerwa, J. Shen and Z. Chen, *Mater. Today Energy*, 2022, **29**, 101098.
169 S. Park, B. Shi, Y. Shang, K. Deng and K. Fu, *Nano Lett.*, 2022, **22**, 9462–9469.
170 Y. Zhao, Q. Zhou, L. Liu, J. Xu, M. Yan and Z. Jiang, *Electrochim. Acta*, 2006, **51**, 2639–2645.
171 H.-Z. Liu, X.-J. Li, Q. Li, X.-X. Liu, F.-J. Chen and G.-H. Zhang, *New Carbon Mater.*, 2022, **37**, 956–967.
172 X. Ye, C. Wang, L. Wang, B. Lu, F. Gao and D. Shao, *Chem. Commun.*, 2022, **58**, 7642–7645.
173 A. Maurel, M. Courty, B. Fleutot, H. Tortajada, K. Prashantha, M. Armand, S. Grugeon, S. Panier and L. Dupont, *Chem. Mater.*, 2018, **30**, 7484–7493.
174 A. Maurel, R. Russo, S. Grugeon, S. Panier and L. Dupont, *ECS J. Solid State Sci. Technol.*, 2021, **10**, 037004.
175 J. Qian, Q. Chen, M. Hong, W. Xie, S. Jing, Y. Bao, G. Chen, Z. Pang, L. Hu and T. Li, *Mater. Today*, 2022, **54**, 18–26.
176 S. Lawes, Q. Sun, A. Lushington, B. Xiao, Y. Liu and X. Sun, *Nano Energy*, 2017, **36**, 313–321.
177 E. Brown, P. Yan, H. Tekik, A. Elangovan, J. Wang, D. Lin and J. Li, *Mater. Des.*, 2019, **170**, 107689.
178 B. Yu, Y. Ji, X. Hu, Y. Liu, J. Yuan, S. Lei, G. Zhong, Z. Weng, H. Zhan and Z. Wen, *Chem. Eng. J.*, 2022, **430**, 132993.
179 K. Shen, B. Li and S. Yang, *Energy Storage Mater.*, 2020, **24**, 670–675.
180 K. Shen, Z. Cao, Y. Shi, Y. Zhang, B. Li and S. Yang, *Energy Storage Mater.*, 2021, **35**, 108–113.

181 Z. Lyu, G. J. H. Lim, R. Guo, Z. Pan, X. Zhang, H. Zhang, Z. He, S. Adams, W. Chen, J. Ding and J. Wang, *Energy Storage Mater.*, 2020, **24**, 336–342.
182 C. Chen, S. Li, P. H. L. Notten, Y. Zhang, Q. Hao, X. Zhang and W. Lei, *ACS Appl. Mater. Interfaces*, 2021, **13**, 24785–24794.
183 H. He, L. Zeng, D. Luo, J. He, X. Li, Z. Guo and C. Zhang, *Adv. Mater.*, 2023, **35**, e2211498.
184 M. Idrees, S. Batool, J. Cao, M. S. Javed, S. Xiong, C. Liu and Z. Chen, *Nano Energy*, 2022, **100**, 107505.
185 P. Liu, Z. Zhang, R. Hao, Y. Huang, W. Liu, Y. Tan, P. Li, J. Yan and K. Liu, *Chem. Eng. J.*, 2021, **403**, 126425.
186 L. Zeng, H. He, H. Chen, D. Luo, J. He and C. Zhang, *Adv. Energy Mater.*, 2022, **12**, 2103708.
187 G. Shi, X. Peng, J. Zeng, L. Zhong, Y. Sun, W. Yang, Y. L. Zhong, Y. Zhu, R. Zou, S. Admassie, Z. Liu, C. Liu, E. I. Iwuoha and J. Lu, *Adv. Mater.*, 2023, **35**, e2300109.
188 H. Wang, D. Lin, Y. Liu, u. Li and Y. Cui, *Sci. Adv.*, 2017, **3**, e1701301.
189 R. Zhang, N. W. Li, X. B. Cheng, Y. X. Yin, Q. Zhang and Y. G. Guo, *Adv. Sci.*, 2017, **4**, 1600445.
190 Y. Yang, L. Ai, S. Yu, J. He, T. Xu, D. Chen and L. Shen, *ACS Appl. Energy Mater.*, 2022, **5**, 15666–15672.
191 Y. Yu, Z. Wang, Z. Hou, W. Ta, W. Wang, X. Zhao, Q. Li, Y. Zhao, Q. Zhang and Z. Quan, *ACS Appl. Energy Mater.*, 2019, **2**, 3869–3877.
192 S. Ni, M. Zhang, C. Li, R. Gao, J. Sheng, X. Wu and G. Zhou, *Adv. Mater.*, 2023, **35**, e2209028.
193 A. Maurel, M. Armand, S. Grugeon, B. Fleutot, C. Davoisne, H. Tortajada, M. Courty, S. Panier and L. Dupont, *J. Electrochem. Soc.*, 2020, **167**, 070536.
194 A. J. Blake, R. R. Kohlmeyer, J. O. Hardin, E. A. Carmona, B. Maruyama, J. D. Berrigan, H. Huang and M. F. Durstock, *Adv. Energy Mater.*, 2017, **7**, 1602920.
195 Q. Chen, R. Xu, Z. He, K. Zhao and L. Pan, *J. Electrochem. Soc.*, 2017, **164**, A1852–A1857.
196 H. Ragones, A. Vinegrad, G. Ardel, M. Goor, Y. Kamir, M. M. Dorfman, A. Gladkikh and D. Golodnitsky, *J. Electrochem. Soc.*, 2019, **167**, 070503.
197 Y. Gambe, H. Kobayashi, K. Iwase, S. Stauss and I. Honma, *Dalton Trans.*, 2021, **50**, 16504–16508.
198 K. Lee, Y. Shang, V. A. Bobrin, R. Kuchel, D. Kundu, N. Corrigan and C. Boyer, *Adv. Mater.*, 2022, **34**, e2204816.
199 K.-S. Ji, H.-S. Moon, J.-W. Kim and J.-W. Park, *J. Power Sources*, 2003, **117**, 124–130.
200 M. Cheng, Y. Jiang, W. Yao, Y. Yuan, R. Deivanayagam, T. Foroozan, Z. Huang, B. Song, R. Rojaee, T. Shokuhfar, Y. Pan, J. Lu and R. Shahbazian-Yassar, *Adv. Mater.*, 2018, **30**, e1800615.
201 Y. He, S. Chen, L. Nie, Z. Sun, X. Wu and W. Liu, *Nano Lett.*, 2020, **20**, 7136–7143.
202 S.-H. Kim, K.-H. Choi, S.-J. Cho, J. Yoo, S.-S. Lee and S.-Y. Lee, *Energy Environ. Sci.*, 2018, **11**, 321–330.
203 D. W. McOwen, S. Xu, Y. Gong, Y. Wen, G. L. Godbey, J. E. Gritton, T. R. Hamann, J. Dai, G. T. Hitz, L. Hu and E. D. Wachsman, *Adv. Mater.*, 2018, **30**, e1707132.
204 S. Zekoll, C. Marriner-Edwards, A. K. O. Hekselman, J. Kasemchainan, C. Kuss, D. E. J. Armstrong, D. Cai, R. J. Wallace, F. H. Richter, J. H. J. Thijssen and P. G. Bruce, *Energy Environ. Sci.*, 2018, **11**, 185–201.
205 H. Xie, Y. Bao, J. Cheng, C. Wang, E. M. Hitz, C. Yang, Z. Liang, Y. Zhou, S. He, T. Li and L. Hu, *ACS Energy Lett.*, 2019, **4**, 2668–2674.
206 J. Qin, P. Das, S. Zheng and Z.-S. Wu, *APL Mater.*, 2019, **7**, 090902.
207 X. Shi, Z. S. Wu, J. Qin, S. Zheng, S. Wang, F. Zhou, C. Sun and X. Bao, *Adv. Mater.*, 2017, **29**, 1703034.
208 X. Lu, T. Zhao, X. Ji, J. Hu, T. Li, X. Lin and W. Huang, *J. Alloys Compd.*, 2018, **760**, 78–83.
209 M. Zhang, T. Hu, X. Wang, P. Chang, Z. Jin, L. Pan, H. Mei, L. Cheng and L. Zhang, *J. Mater. Chem. A*, 2022, **10**, 7195–7206.
210 S. Praveen, T. Kim, S. P. Jung and C. W. Lee, *Small*, 2023, **19**, e2205817.
211 E. Cohen, S. Menkin, M. Lifshits, Y. Kamir, A. Gladkich, G. Kosa and D. Golodnitsky, *Electrochim. Acta*, 2018, **265**, 690–701.
212 W. Gao and M. Pumera, *Adv. Funct. Mater.*, 2021, **31**, 2007285.
213 Y. Liu, Y. Qiao, Y. Zhang, Z. Yang, T. Gao, D. Kirsch, B. Liu, J. Song, B. Yang and L. Hu, *Energy Storage Mater.*, 2018, **12**, 197–203.
214 T. S. Wei, B. Y. Ahn, J. Grotto and J. A. Lewis, *Adv. Mater.*, 2018, **30**, e1703027.
215 C. Kim, B. Y. Ahn, T. S. Wei, Y. Jo, S. Jeong, Y. Choi, I. D. Kim and J. A. Lewis, *ACS Nano*, 2018, **12**, 11838–11846.
216 X. Yu, Y. Liu, H. Pham, S. Sarkar, B. Ludwig, I.-M. Chen, W. Everhart, J. Park, Y. Wang and H. Pan, *Adv. Mater. Technol.*, 2019, **4**, 1900645.
217 C. Reyes, R. Somogyi, S. Niu, M. A. Cruz, F. Yang, M. J. Catenacci, C. P. Rhodes and B. J. Wiley, *ACS Appl. Energy Mater.*, 2018, **1**, 5268–5279.
218 L. Zhou, W. Ning, C. Wu, D. Zhang, W. Wei, J. Ma, C. Li and L. Chen, *Adv. Mater. Technol.*, 2018, **4**, 1800402.
219 K. Xu, N. Zhao, Y. Li, P. Wang, Z. Liu, Z. Chen, J. Shen and C. Liu, *Electrochem. Commun.*, 2022, **139**, 107312.
220 C. C. Ho, K. Murata, D. A. Steingart, J. W. Evans and P. K. Wright, *J. Manuf. Syst.*, 2009, **19**, 094013.
221 A. Pendashteh, J. Palma, M. Anderson, J. J. Vilatela and R. Marcilla, *ACS Appl. Energy Mater.*, 2018, **1**, 2434–2439.
222 Y. Ding, J. Cai, Y. Sun, Z. Shi, Y. Yi, B. Liu and J. Sun, *ACS Nano*, 2022, **16**, 3373–3382.
223 F. Degen, M. Winter, D. Bendig and J. Tübke, *Nat. Energy*, 2023, 1–12, DOI: **10.1038/s41560-023-01355-z**.
224 X. Wang, H. Huang, F. Zhou, P. Das, P. Wen, S. Zheng, P. Lu, Y. Yu and Z.-S. Wu, *Nano Energy*, 2021, **82**, 105688.
225 Y. Bao, Y. Liu, Y. Kuang, D. Fang and T. Li, *Energy Storage Mater.*, 2020, **33**, 55–61.
226 Y. Li, Y. Wang, Y. Liu, Z. Lin, Z. Ye, J. Wang, J. Qiu, H. Zhang and G. Cao, *Energy Storage Mater.*, 2023, **57**, 497–507.
227 S. Praveen, G. S. Sim, C. W. Ho and C. W. Lee, *Energy Storage Mater.*, 2021, **41**, 748–757.

228 D. Ji, H. Zheng, H. Zhang, W. Liu and J. Ding, *Chem. Eng. J.*, 2022, **433**, 133815.
229 X. Tang, D. Zhou, B. Zhang, S. Wang, P. Li, H. Liu, X. Guo, P. Jaumaux, X. Gao, Y. Fu, C. Wang, C. Wang and G. Wang, *Nat. Commun.*, 2021, **12**, 2857.
230 Y. Liang, H. Dong, D. Aurbach and Y. Yao, *Nat. Energy*, 2020, **5**, 646–656.
231 K. T. Braam, S. K. Volkman and V. Subramanian, *J. Power Sources*, 2012, **199**, 367–372.
232 H. Wang, R. Guo, H. Li, J. Wang, C. Du, X. Wang and Z. Zheng, *Chem. Eng. J.*, 2022, **429**, 132196.
233 H. Ma, X. Tian, J. Fan, W. Cao, X. Yuan, S. Hou and H. Jin, *J. Power Sources*, 2022, **550**, 232152.
234 W. Yan, X. Cai, F. Tan, J. Liang, J. Zhao and C. Tan, *Chem. Commun.*, 2023, **59**, 1661–1664.
235 Y. Ren, F. Meng, S. Zhang, B. Ping, H. Li, B. Yin and T. Ma, *Carbon Energy*, 2022, **4**, 446–457.
236 Y. Lin, J. Chen, M. M. Tavakoli, Y. Gao, Y. Zhu, D. Zhang, M. Kam, Z. He and Z. Fan, *Adv. Mater.*, 2019, **31**, 1804285.
237 F. Zhang, M. Wei, V. V. Viswanathan, B. Swart, Y. Shao, G. Wu and C. Zhou, *Nano Energy*, 2017, **40**, 418–431.
238 D. B. Ahn, S.-S. Lee, K.-H. Lee, J.-H. Kim, J.-W. Lee and S.-Y. Lee, *Energy Storage Mater.*, 2020, **29**, 92–112.
239 J. Zhao, H. Lu, X. Zhao, O. I. Malyi, J. Peng, C. Lu, X. Li, Y. Zhang, Z. Zeng, G. Xing and Y. Tang, *ACS Mater. Lett.*, 2020, **2**, 1041–1056.
240 L. Zeng, J. He, C. Yang, D. Luo, H. Yu, H. He and C. Zhang, *Energy Storage Mater.*, 2023, **54**, 469–477.
241 K.-H. Lee, S.-S. Lee, D. B. Ahn, J. Lee, D. Byun and S.-Y. Lee, *Sci. Adv.*, 2020, **6**, eaaz1692.
242 M. Rafiee, R. D. Farahani and D. Therriault, *Adv. Sci.*, 2020, **7**, 1902307.
243 J. Ma, J. Qin, S. Zheng, Y. Fu, L. Chi, Y. Li, C. Dong, B. Li, F. Xing, H. Shi and Z. S. Wu, *Nano-Micro Lett.*, 2024, **16**, 67.
244 X. Li, S. Ling, W. Cao, L. Zeng, R. Yuan and C. Zhang, *Angew. Chem., Int. Ed.*, 2022, **61**, e202202663.
245 S. Zheng, J. Ma, K. Fang, S. Li, J. Qin, Y. Li, J. Wang, L. Zhang, F. Zhou, F. Liu, K. Wang and Z. S. Wu, *Adv. Energy Mater.*, 2021, **11**, 2003835.